Mobility of dry granular ~~debris~~ flows over erodible beds: Experimental insights into the influence of flow–bed ~~inertia~~density contrasts

Katharina Wetterauer[1], Sebastian Müller[2], Michael Krautblatter[3], Shiva P. Pudasaini[3], and Ivo Baselt[1]

[1]Mountain River Research Group, University of the Bundeswehr Munich, Neubiberg, Germany
[2]Chair of Hydromechanics and Hydraulic Engineering, University of the Bundeswehr Munich, Neubiberg, Germany
[3]Chair of Landslide Research, Technical University of Munich, Munich, Germany

Correspondence: Katharina Wetterauer (katharina.wetterauer@unibw.de)

Abstract. ~~Debris-flow mobility responds sensitively to erosion and entrainment that~~ Erosion and entrainment exchange mass and momentum across the ~~flow-bed interface . Yet, the mechanical controls that cause some debris flows to accelerateduring erosion while others deceleratеare~~ flow–bed interface and can strongly modify debris-flow mobility. However, the material properties that control whether erosive flows accelerate, decelerate, or maintain their mobility remain insufficiently understood. ~~Recent theory attributes this divergent behavior to inertial contrasts between the~~ Here, we conducted dry granular flow experiments to investigate how contrasts in solid particle density between a moving mass and ~~the erodible bed , suggesting that incorporating inertially weaker, neutral, or stronger substrate into the flow enhances, maintains, or reduces flow mobility, respectively. Here, we conducted flume experiments and surface-based measurements to assess how the inertia of the erodible bed affects the flow kinematics, erosion, entrainment, and runout of dry granular single-phase debris flows. We systematically imposed inertial contrasts by releasing a~~ an erodible bed affect erosion, flow evolution, and deposition, using surface measurements of the evolving flow and final deposit. A quartz slide of constant solid ~~density over erodible~~ particle density was released over beds with lower, equal, and higher solid ~~densities representing inertially weak, neutral, and strong scenarios, and compare these alongside~~ particle densities and compared with a reference case without erosion. Each scenario was repeated ~~for fine sand and a sand–gravel mixture. Our results reveal consistent behavior across both particle-size distributions. Debris flows over~~ using finer sand-sized particles and coarser sand-to-gravel-sized particles. The low-density beds ~~exhibit higher apparent mean erosionrates, faster flow fronts before deposition~~produced deeper erosion, higher average flow-front velocities, and longer runout~~lengths, whereas flows over~~ . By contrast, the equal- and high-density beds ~~evolve similarly~~produced nearly identical results, with shallower erosion ~~, slower flow fronts, and shorter,~~ depths, lower average flow-front velocities, and more compact deposits, despite their substantially different solid particle densities. The same relative patterns were observed for both particle-size fractions, although coarse-particle flows generally formed longer and flatter deposits. ~~Relative to the neutral scenario, the entrainment of low-density material thus appears to enhance debris-flow mobility, while incorporating high-density material does not lead to the anticipated mobility loss.~~ This asymmetric response ~~suggests that solid-density contrasts aloneare insufficient to explain the observed trends under the experimental conditions considered here. Differences in particle shape and internal friction likely~~

also contribute. Whereas the shows that mobility cannot be explained by solid particle density alone. Instead, the enhanced mobility over the low-density bed comprises more spherical particles with a lower friction angle facilitating entrainment, beds is more consistently explained by coupled effects of lower internal friction, rounded particle shape, greater bed deformation, and more efficient entrainment. The similar response of the equal- and high-density beds consist of angular particles with similar and higher internal friction angles, leading apparently to similar resistance to erosion despite their divergent densities. However, resolving reflects their comparable and higher frictional resistance and angular particle shape, which appear to outweigh the contrast in solid particle density under the tested conditions. Yet, surface-based measurements alone cannot resolve whether more subtle differences persist between the inertial scenarios will require direct in basal slip, shear localization, and the incorporation of mobilized bed material. Depth-resolved observations at the flow–bed interface to capture grain-scale dynamics and temporal variability in erosion intensity.

are therefore needed to directly relate erosion and entrainment to mass and momentum exchange.

1 Introduction

Debris flowsare highly dynamic natural hazards that Gravity-driven mass movements in steep terrain, including dry granular flows, rock avalanches, and debris flows, shape mountain landscapes through erosion, entrainment, transport, and deposition. Understanding their flow dynamics is By entraining bed sediment, especially on metastable slopes (Mangeney et al., 2010; Mangeney, 2011; Aaron and McDougall, 2019), such flows can rapidly increase in volume and mobility (Hungr and Evans, 2004). Understanding flow–bed interactions is therefore essential for predicting future debris-flow activity in a changing climate mass-flow dynamics and hazards under changing climatic conditions and for reconstructing long-term landscape evolution (e.g., Rickenmann, 1999; Reid et al., 2011; Roelofs et al., 2023). YetDespite their importance, the physical mechanisms behind the high mobility observed in some erosive debris flows remain debated. Erosion of sediment from the bed and entrainment into the flow are thought to play a key role because they modify the total flow volume and can influence governing mobility in erosive flows remain incompletely understood (e.g., De Haas and Van Woerkom, 2016; Pudasaini and Fischer, 2020; Jiang et al., 2023). In general, entrainment alters mobility through mass and momentum transfer, changes in basal resistance, and bed weakening (e.g., Hungr et al., 2005; Mangeney et al., 2007; Santi et al., 2008; Iverson et al., 2011). However, Yet, mobility responses are not uniform: some debris flows disproportionally increase their volume and become highly mobile and destructive through entrainment. Some erosive flows become more mobile as bed material is entrained, whereas others decelerate despite eroding . Processes of erosion locally during erosion without necessarily exhibiting lower overall mobility (e.g., Hungr et al., 2005; Mangeney et al., 2007; Farin et al., 2014; Zhang et al., 2026).

Erosion and entrainment are increasingly incorporated into debris-flow mobility models, accounting for mass production mechanical mass flow models. Existing approaches account for flow-volume growth (e.g., McDougall and Hungr, 2005; Medina et al., 2008; Iverson, 2012; Frank et al., 2015) and mechanically including momentum production . However, the lack of a unified erosion theory and the mechanical complexity of mechanical effects on the momentum balance, including basal shear

resistance and flow–bed ~~interactions still lead to large discrepancies among model equations and outcomes . Additionally, many debris-flow models rely on poorly constrained equations or parameters, highlighting the need for data obtained under controlled and reproducible conditions~~ momentum exchange over erodible beds (e.g., Takahashi, 1991; Iverson, 2012; Takahashi, 2014; Iverson and Ouyang, 2015; Pudasaini and Fischer, 2020). However, numerical models differently represent entrainment. Depth-averaged simulations commonly prescribe erosion through entrainment laws based on basal shear stress, whereas alternative formulations consider slope-normal or tangential momentum jumps and frontal ploughing (Issler, 2014, 2020). By contrast, depth-resolved simulations represent both the moving mass and the erodible bed through constitutive laws. Erosion and entrainment can therefore emerge from the evolving stress and deformation fields rather than from separate closure assumptions for entrainment fluxes and boundary stresses (e.g., Crosta et al., 2009). Fully three-dimensional depth-resolved simulations have become increasingly feasible at slope scale (Cicoira et al., 2022; Kyburz et al., 2025; Zhu et al., 2025). Across these modeling approaches, there is a growing need for controlled experimental datasets against which predictions of erosion, entrainment, and mobility can be evaluated (Iverson et al., 2011; De Haas et al., 2020).

Controlled flume experiments have ~~helped to constrain key parameters that correlate with the erosion potential of debris flows, primarily by systematically varying either the initial flow conditions or the bed characteristics while keeping the other constant. For example, when flow conditions are varied, granular single-phase flow experiments show that a greater~~ identified both flow-related and bed-related controls on erosion and entrainment. Dry granular flow experiments using broadly similar flow and bed materials show that erodible layers can either enhance or reduce mobility depending on boundary conditions (Crosta et al., 2009; Mangeney et al., 2010). Among the investigated flow-related controls, greater released mass intensifies bed erosion and entrainment (Lu et al., 2016) and enlarges the eroded zone, ~~resulting in higher mobility and longer~~ with associated increases in mobility and runout (Liu et al., 2023). Two-phase debris-flow experiments further ~~reveal~~ indicate that water- or gravel-rich flows are more erosive than clay-rich flows (De Haas and Van Woerkom, 2016; Roelofs et al., 2022)~~, with erosion largely controlled by~~ . In these experiments, erosion has been related to both basal shear stress (De Haas and Van Woerkom, 2016) ~~. Erosion increases linearly with higher water and gravel contents, as pore-pressure transfer to the bed and impact forces are enhanced, respectively. Increasing clay content, however, alters interstitial fluid viscosity and pore-pressure dynamics, leading to a non-linear erosion response . Runout analyses additionally indicate that higher water content increases entrainment volume, producing~~ and collisional stresses (De Haas et al., 2022; Zheng et al., 2025). Increasing the water content of the moving material may additionally increase entrainment volumes and produce flatter, wider, and longer deposits (Pandey and Satyam, 2025). ~~Instead, varying the bed characteristics demonstrates also the role of the mechanical and hydraulic properties of the erodible substrate. Erosion rates decrease as bed sediment becomes coarser~~ Among the investigated bed-related controls, erosion rates decrease with increasing bed grain size (Egashira et al., 2001; Papa et al., 2004). ~~Small-scale and large-scale experiments show that increasing~~ Increasing bed water content~~facilitates bed~~ , by contrast, facilitates entrainment through elevated ~~pore~~ pore-water pressures and reduced ~~effective basal friction, promoting higher flow velocities, mass and momentum growth, and longer runout. Measurements from natural events support these findings, indicating that high~~ internal friction, as observed in both small-scale (Roelofs et al., 2023) and large-scale experiments (Reid et al., 2011; Iverson et al., 2011). Field observations support the experimentally observed role of bed saturation. High bed pore-water ~~pressures within the bed~~

coincide with sediment-entrainment phases pressures coincide with phases of sediment entrainment (Berger et al., 2011)and that debris , and flows over saturated beds grow faster and attain more volume larger volumes than those over drier beds (McCoy et al., 2012). Besides, variations in bed clay content appear to influence the contraction–dilation behavior of the bed , with an optimum clay content at which undrained loading conditions and liquefaction of the upper bedlayer produce maximum erosion . Overall, these experimental insights highlight the mechanical complexity of processes across the recent experiments further indicate that dry granular flow–bed interface, which current theoretical models only partially capture.

A recent theoretical mobility model, proposed by , offers a mechanical explanation that links the erosion and mobilityof landslides through bed inertia. For effectively single-phase flows, their approach derives mobility from the fundamental balance equations of mass, momentum, and energy rather than from empirical correlations. In this framework, erosion not only increases the landslide volume but also alters the energy budget of the moving mass by changing its inertia interactions may also vary spatially along the erodible bed (Zhang et al., 2026). Whereas impact-induced ploughing and compression dominate the proximal bed, shear-dominated entrainment prevails farther downslope. These findings imply that erosion may either dissipate flow momentum or enhance mobility, depending on the mechanical properties of the entrained bed sediment. According to the model, three distinct energy regimes arise from the inertial contrast efficiency of bed entrainment.

Among the experimentally investigated flow and bed properties, the role of contrasts in solid particle density between the moving slide flow and the erodible bed . Mobility remains unchanged when erosion proceeds under inertially neutral conditions, where the slide and bed material exhibit equal inertia and no net gain or loss of flow momentum and energy occurs. In contrast, mobility increases through the erosion of an inertially weaker bed, which introduces mechanically weaker material into the moving slide, enhancing flow momentum and energy. Conversely, mobility decreases through the erosion of an inertially stronger bed, as mechanically stronger material is entrained into the slide, causing momentum and energy dissipation despite continued erosion and volume gain. Accordingly, these contrasting energy regimes would directly govern landslide runout, as mobility gain or loss results in longer or shorter travel distances. Although this formulation provides a clear mechanical basis for how and when erosion enhances or reduces landslide mobility , the predicted processes have not yet been empirically confirmed and parameterized.

The present study examines how variations in bed inertia influence the mobility and runout of erosive debris flows in a series of small-scale flume experiments. We conducted dry granular single-phase debris-flow experiments in a steep channel, systematically varying the inertial contrast between sliding and bed material. We tested remains poorly constrained. Such contrasts may arise from lithological differences and can be particularly pronounced during interactions between rock-rich masses and snow or glacier ice (Mergili et al., 2020; Feng et al., 2023; Munch et al., 2024; Yang et al., 2025; Peng et al., 2025). In many natural settings, however, contrasts in solid particle density may be modest. They also commonly coincide with differences in particle-size distribution, particle shape, porosity, packing, water or ice content, bed strength, and frictional resistance. This covariance makes the isolated mechanical contribution of solid particle density difficult to determine. Still, solid particle density is mechanically relevant because it determines bulk density together with porosity or solid volume fraction. Bulk density, in turn, governs mass and momentum balances, normal and shear stresses, and flow–bed momentum exchange

in mechanical models (e.g., Takahashi, 1991; Iverson, 2012; Takahashi, 2014; Iverson and Ouyang, 2015). Previous flume experiments show that bed bulk density can influence erosion and mobility when altered through compaction and porosity (Farin et al., 2014). Yet, these experiments did not isolate the contribution of solid particle density itself. The theoretical mobility model of Pudasaini and Krautblatter (2021) likewise considered density contrast as a potential control and motivated the present experimental design. Subsequent discussion addressed mainly the specific kinematic assumptions of the model, particularly the velocity assigned to erodible bed material (Issler et al., 2024), rather than the potential mechanical role of density contrasts. Controlled experiments are therefore needed in which other material properties are kept as similar as possible while the contrast in solid particle density is sufficiently large to produce a measurable response.

To address this gap, we designed a series of dry granular flow experiments in which a constant quartz slide was released over erodible beds with lower, equal, and higher solid particle density relative to the slide. These three erosive scenarios ~~that represent inertially weak, neutral, and strong conditions, as well as a reference scenario without erosion. Each scenario was performed for a~~ were compared to a non-erosive reference scenario with rigid bed and investigated for both finer (sand-sized) and ~~a~~ coarser (sand-to-gravel-sized) ~~fraction to assess potential grain-size-dependent effects. We combine~~ particles. Within each particle-size fraction, particle-size distributions were kept comparable across scenarios to minimize accompanying variations in porosity. Although solid-particle-density contrast was the primary design variable, accompanying sediment properties such as particle shape and frictional resistance could not be controlled fully independently in all cases. We therefore interpret the experiments as controlled density contrast scenarios in which accompanying material properties are explicitly considered. By combining high-resolution measurements of flow surface and deposit ~~surface~~ topography with qualitative analyses of the ~~deposit's internal structure. This integrated analysis directly relates debris-flow dynamics, erosion intensity, and depositional form, to assess from different stages of the event how erosion at mechanically contrasting flow–bed interfaces affects flow mobility. Our empirical findings therefore provide a first-order, surface-based evaluation of how the inertia-based mobilityconcept proposed by aligns with experimentally observed debris-flow behavior~~internal deposit structure, we assess how contrasting bed materials affect erosion, average flow-front velocity, deposit morphology, and internal sorting. These experiments provide benchmark data for testing whether numerical models can reproduce material-dependent erosion, mobility, and deposition of dry granular flows.

2 Material and Methods

2.1 Targeted ~~inertial~~ density contrast scenarios and materials

~~Inertia describes the resistance of moving material to a change of its velocity in magnitude and direction. In continuum mechanics, inertia is, beside velocity, proportional to mass density for a given material volume. Consequently, debris-flow inertia can be modified by incorporating mass from an erodible bedwith a different density, solid volume fraction, friction, or different velocity. To test the inertia-based mobility concept proposed by , we designed a setup for dry granular debris-flow~~

experiments, where the dry debris flow overrides a dry erodible bed initially at rest. In the present study, any change in inertia can therefore only arise from a change in density. Based on this density–inertia relationship, we use sliding materials and erodible beds that exhibit distinct contrasts in solid densityThe experiments were designed as controlled density contrast scenarios between a dry granular slide and a dry granular erodible bed. Accordingly, materials with higher density are considered inertially (mechanically) stronger, whereas low-density materials are considered inertially (mechanically) weaker. As this study provides an initial experimental assessment of the hypotheses by and focuses on testing the predicted mechanical behavior under controlled dry granular conditions, we do not aim to achieve full dynamic similarity with natural debris flows. Instead, all analyses are conducted Unconsolidated quartz grains were used as the released slide material in all experiments, whereas the erosive bed material had systematically lower, equal, or higher solid particle density. Particle-size distribution, initial bed geometry, and packing were kept comparable across experiments to minimize systematic differences in porosity. Consequently, differences in dry bulk density primarily reflect differences in solid particle density rather than intentionally varied bed structure. The experiments were performed at a consistent laboratory scale , and our interpretations are based on relative differences between weak, neutral, and strong scenarios rather than on absolute scaling to natural debris flowsand were not intended as dynamically scaled reproductions of natural flows. Accordingly, the imposed solid-particle-density contrasts were deliberately larger than those typically expected in natural torrent or hillslope materials in order to produce measurable differences in flow response.

Four slide–bed configurationscalled "scenarios" were testedby keeping the initial sliding material constant while systematically varying the bed material, hereafter referred to as scenarios, were tested: (i) an inertially weak a low-density scenario, where a quartz slide overrode a low-density bed made of expanded glass with a lower solid particle density ($\rho_{\mathrm{Glass}} \approx 400$–$600\ \mathrm{kg\,m^{-3}}$; Fig. 1a),; (ii) an inertially neutral equal-density scenario, where both slide and bed consisted of quartz with equal solid particle density ($\rho_{\mathrm{Qtz}} = 2700\ \mathrm{kg\,m^{-3}}$; Fig. 1b),; (iii) an inertially strong a high-density scenario, where a quartz slide overrode a high-density bed made of magnetite with a higher solid particle density ($\rho_{\mathrm{Mag}} = 4800\ \mathrm{kg\,m^{-3}}$; Fig. 1c),; and (iv) a reference scenario without erosionnon-erosive reference scenario, where the quartz slide moved over a rigid, rough-coated plywood surface (rough plywood plate (equivalent sand roughness $k_s \approx 0.27$ mm; Fig. 1d). In the three erosive scenarios (i–iii), the quartz thus served as the inertial solid-particle-density reference relative to the erodible bed material (Table 1). Its initially released volume mass was identical in all experiments and consisted of 130 kg dry quartz sand (Fig. 1b). In addition, to examine whether potential inertial effects vary across particle-size fractions,

Each of the four scenarios were each was conducted in two experimental series using a fine fraction (differing in particle size (Fig. 1). In a fine series ("/f"), both the initially released slide and the erodible bed consisted of a finer 0.25–2 mm ; "/f")composed of fraction, comprising 100% sand, and a coarse fraction (% sand-sized particles. In a coarse series ("/c"), slide and bed consisted of a coarser 0.25–8 mm ; "/c")composed of fraction, comprising 50% sand sand-sized and 50% gravel (Fig. 1e).

Materials used to simulate different inertial bed conditions in the conducted debris-flow experiments. (a-c) Erodible bed materials with (a) expanded glass for the inertially weak scenario, (b) quartz for the inertially neutral scenario, and (c) magnetite

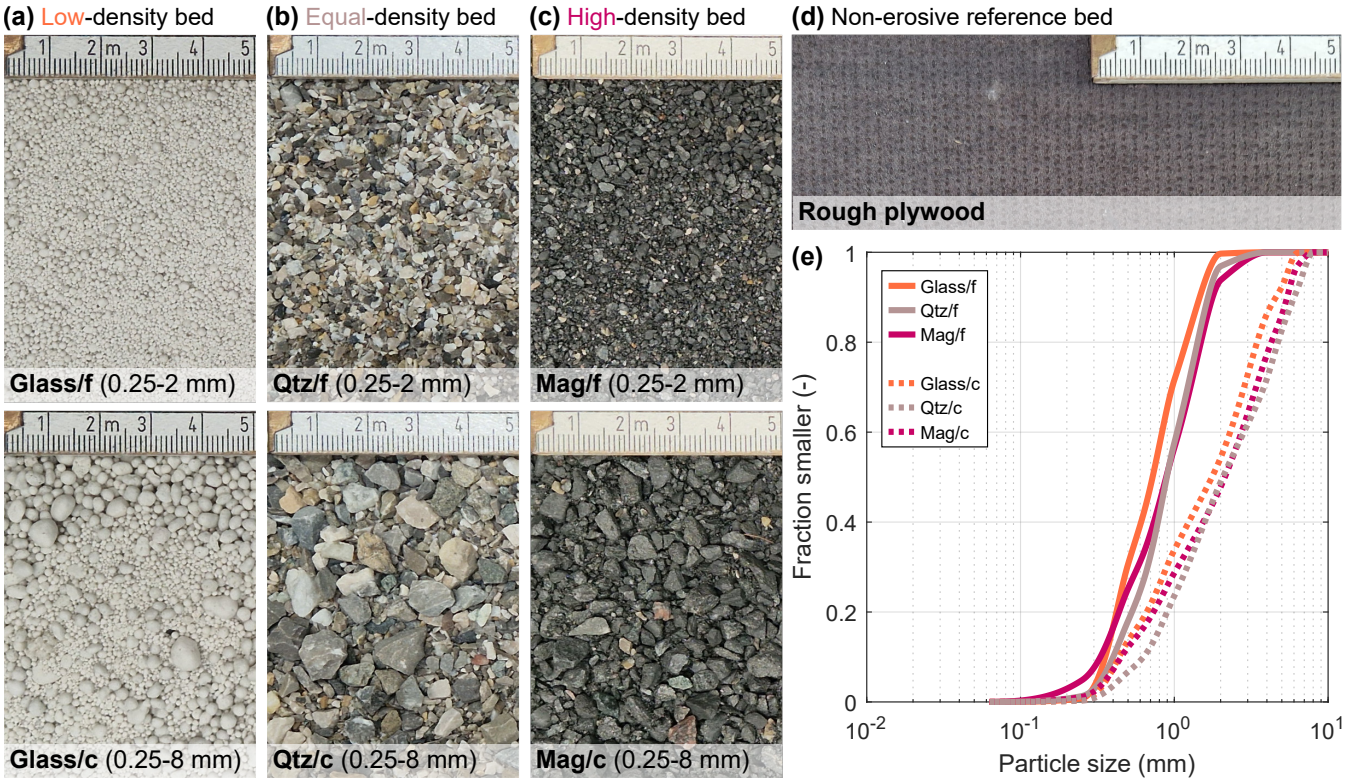


Figure 1. Materials used to study the influence of solid-particle-density contrasts in the dry granular flow experiments. (a-c) Erodible bed materials with (a) expanded glass (Glass) for the low-density scenario, (b) quartz (Qtz) for the equal-density scenario, and (c) magnetite (Mag) for the high-density scenario. (d) Rough plywood used as rigid bed for a non-erosive reference. (e) Cumulative particle-size distributions. Note that Qtz/f and Qtz/c shown in (b) were also used as initial sliding material in the corresponding fine- or coarse-particle experiments. /f: fine particles; /c: coarse particles.

~~for the inertially strong scenario. (d) Coated plywood plate used as rigid bed for a reference case without erosion. (e) Cumulative particle-size distributions for fine (/f) and coarse (/c) fraction. Note that the quartz sand shown in (b) was used as initial sliding material in all experiments.~~

~~The selection of materials was based on two main considerations: the use of natural sands to approximate the particle characteristics of natural debris-flow sediments, and the ability to efficiently separate slide–bed mixtures after the experiments to enable complete material reuse. Quartz and magnetite were chosen as natural sediments with angular particlesand contrasting densities, and as they allowed efficient post-experimental magnetic separation of their mixture (Table 1, Fig. 1b, c). Expanded glass (PORAVER®), in contrast, is an artificial material composed of nearly spherical particles (Table 1, Fig. 1a). It was selected because no natural sediment with a distinctly lower density relative to quartz was available that could be efficiently separated for reuse. The buoyancy of the light expanded glass enabled complete separation of quartz–glass mixtures by their density contrast in a water bath.~~ gravel-sized particles. To ensure comparable particle-size distributions, quartz, ~~expanded~~ glass, and magnetite

were each sieved into the ~~previously defined fine and coarse~~ corresponding fine- and coarse-particle fractions (Fig. 1e). ~~Detailed material properties are listed in Table 1.~~

From here on, we refer to the materials as “Glass”, “Qtz”, and “Mag”. In the fine series, “Glass/f”, “Qtz/f”, “Mag/f” denote the erosive scenarios and "reference" the non-erosive scenario. In the coarse series, the corresponding experiments are denoted as “Glass/c”, “Qtz/c”, “Mag/c”, and “reference”. Moreover, we use the term “slide” to refer specifically to the initially released Qtz–slide before its interaction with the erodible bed or to distinguish the overrunning from the erodible material.

Table 1. Characteristics of the ~~erodible~~ materials used to simulate the different ~~inertial bed~~ density contrast scenarios. /f: fine particles; /c: coarse particles.

~~Erodible bed~~Scenario ~~material~~	~~Relative inertia~~Bed material ~~of bed to slide~~	Particle size (mm)	Solid particle density ($kg\ m^{-3}$)	Dry bulk density ($kg\ m^{-3}$)	Internal~~friction~~ friction angle (°)	Basal~~friction angle~~[c]friction angle[b] (°)
Low density	Expanded Glass	~~inertially weak~~ Glass/f 0.25–2	580	300	~~20.0~~ 29°	~~25.0~~ 25°
		Glass/c 0.25–8	440	260	~~31.0~~ 31°	~~23.0~~ 23°
Equal density	Quartz	~~inertially neutral~~ Qtz/f[a] 0.25–2	2710	1360	37	31
		Qtz/c[a] 0.25–8	2740	1530	39	30
High density	Magnetite	~~inertially strong~~ Mag/f 0.25–2	4760	2620	35	29
		Mag/c 0.25–8	4830	2750	38	29

~~a~~ Qtz/f and Qtz/c were also used as initial sliding material in the corresponding fine- or coarse-particle experiments.
[b] Angle with respect to the ~~coated~~ rough plywood plates used as rigid bed surface in the flume setup.
~~a~~ Due to the low friction angles, Glass was mixed with 1–5% water to stabilize and prevent self-induced failure on the 37°-inclined flume. [c] Due to the low friction angles, Glass was mixed with 4–5% water by mass to prevent self-induced failure on the 37° inclined flume.

~~From here on , we refer to the materials as “Glass”, “Qtz”, and “Mag”, and to~~ The selection of materials was based on two main considerations. The materials had to show particle characteristics relevant to natural dry granular flows, and the ~~four scenarios as “Glass/f”, “Qtz /f”, “Mag /f”, and “reference” for the fine-particle experiments or “Glass/c”, “Qtz/c”,“Mag/c”,~~ slide–bed mixtures had to be efficiently separable after the experiments to enable complete material reuse. Qtz and Mag were chosen as natural sediments with angular particles and significantly contrasting solid particle densities. Their similar particle shape and frictional properties made them suitable for comparing equal- and ~~“reference” for the coarse-particle experiments. Moreover, we use the term “slide” to refer specifically to the initially released Qtz–slide before its interaction with the erodible bed or to distinguish the overrunning from the erodible material~~ high-density scenarios while minimizing differences in other particle characteristics (Table 1, Fig. 1b, c). In addition, the deposited mixtures of Qtz and the ferromagnetic Mag could be efficiently separated magnetically after each experiment. The Glass (PORAVER®), in contrast, is an artificial material composed of nearly spherical particles (Table 1, Fig. 1a). It was selected because no natural sediment with a distinctly lower solid particle density relative to Qtz was available that could be efficiently separated for reuse. The buoyancy of the light Glass enabled complete separation of Qtz–Glass mixtures by their density contrast in a water bath. ~~In all other cases we use “debris flow”. We further emphasize that , for simplicity and as an initial step, all experiments were conducted in a dry state, representing single-phase flows.~~ Accordingly, ~~when the term “debris flow” refers to our tests, it specifically denotes these dry granular single-phase flows.~~ the low-density scenario provides the intended solid-particle-density contrast relative to the equal-density scenario. However, the two scenarios also differ in particle shape and frictional properties. These material properties are quantified in Table 1 and are explicitly considered in the interpretation of the experimental results.

2.2 Experimental flume

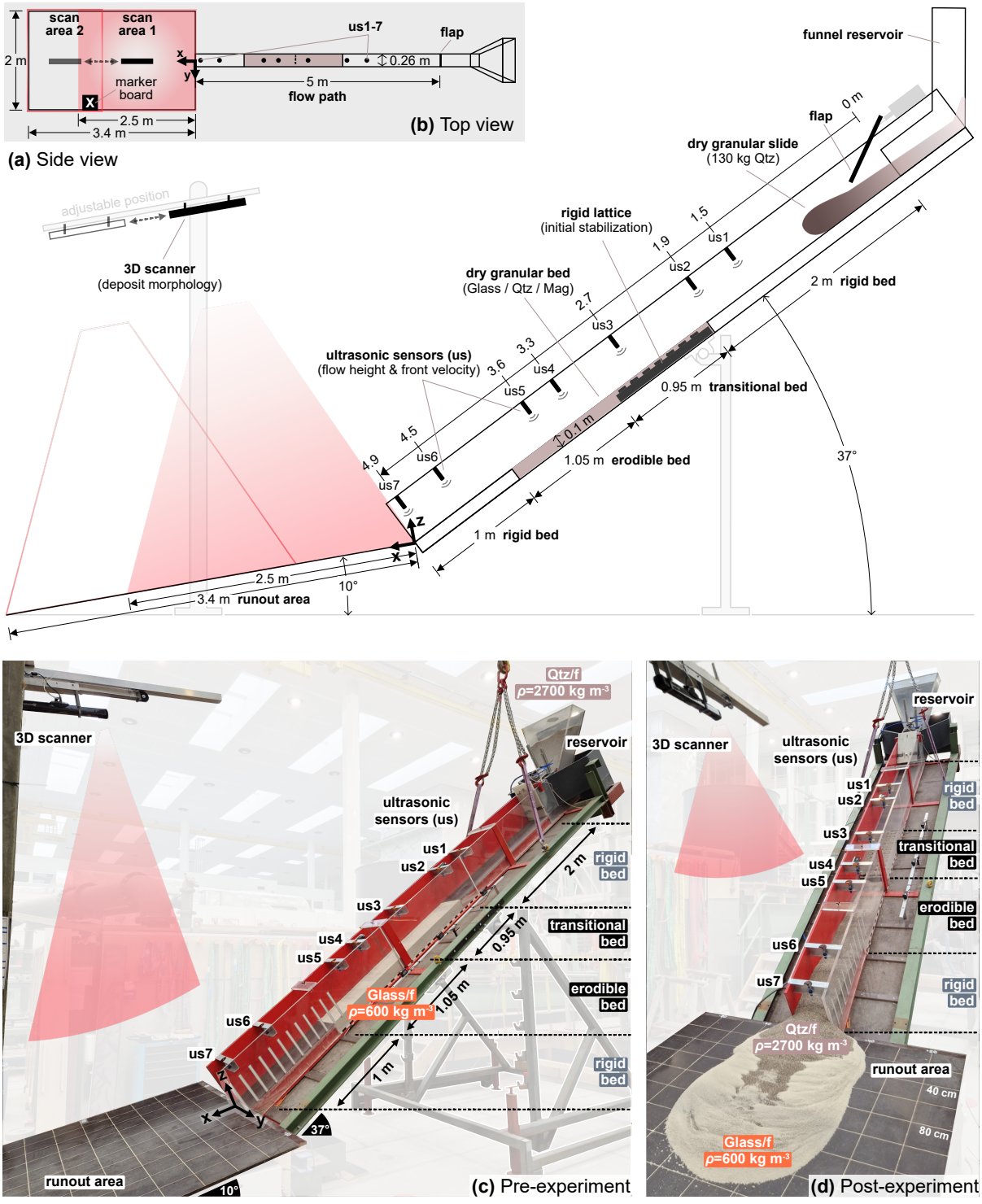


Figure 2. Experimental flume setup. (a) Side- and (b) top-view schematic. (c) Flume with planar erodible bed and filled reservoir before the experiment. (d) Deposit after the experiment. Flume sections and measurement positions are indicated. Photographs are from Exp5 (Glass/f).

~~Debris-flow~~ Dry granular flow experiments were conducted at the Hydraulic Laboratory of the University of the Bundeswehr Munich, Germany, in a newly designed experimental ~~debris-flow~~ flume (Fig. 2). This flume consisted of a 5 m long and 0.26 m wide straight channel with 0.5 m high vertical sidewalls, forming a rectangular cross-section. Upstream of the channel, a funnel-shaped reservoir stored the 130 kg initial sliding material. ~~It~~ This mass corresponded to a calculated release volume of ~96 L for the fine- and ~85 L for the coarse-particle experiments. The reservoir was filled by releasing Qtz vertically from a bag into the reservoir ~~without~~ avoiding pre-mixing to preserve natural variability and internal sorting~~, as these conditions better represent natural debris-flow initiation where material is rarely homogeneous~~. A flap operated by a pneumatic cylinder opened ~~in a split second~~instantaneously, releasing the ~~Qtz~~ initial Qtz–slide into the channel. The 5 m long channel was divided into four distinct sections: (i) an upper rigid bed (2 m) made of ~~rough-coated~~ rough plywood, to allow the slide to develop and accelerate; (ii) a transitional bed (~1 m) containing a rigid lattice ~~,~~ shaped like a ~~Lego~~ LEGO® brick, which was overfilled with erodible bed material to gradually adapt the slide to the erodible bed and prevent immediate scouring at its upstream edge (e.g., De Haas and Van Woerkom, 2016); (iii) an erodible bed (~1 m) with a thickness of 0.1 m; and (iv) a lower rigid bed (1 m) made of ~~rough-coated~~ rough plywood, to avoid extensive head erosion and sudden failure of the erodible bed section. Downstream of the channel, the slide–bed mixture entered a 3.4 m long and 2 m wide runout area~~,~~. This area was inclined by 10° to facilitate material outflow and reduce in-channel deposition ~~resulting from~~ caused by the abrupt slope break and associated reduction ~~of~~ in flow momentum. Except for the channel beds, all flume elements in contact with the flow were made of smooth materials with similarly low roughness ~~(equivalent sand roughness $k_s \leq 0.01$)~~ to minimize frictional resistance. Acrylic glass ($k_s \leq 0.01$ mm) was used for the reservoir and transparent front sidewall, PVC ($k_s \leq 0.01$ mm) for the back sidewall, and smooth plywood ($k_s \approx 0.04$ mm) for the runout area. In contrast, the rigid bed sections were made of rough plywood ($k_s \approx 0.27$ mm; Fig. 1d). Surface roughness was measured using a Keyence VK-X3000 3D laser scanning microscope based on focus variation (<3 µm accuracy). The peak-to-valley roughness R_z was determined along a circle on the respective surface and is reported here because it closely approximates the equivalent sand roughness k_s (Adams et al., 2012).

~~A steep~~ A flume inclination of 37° was used for all dry granular flow experiments to ensure sufficiently high sliding velocities and ~~, therefore, a high~~ erosive potential (e.g., De Haas and Van Woerkom, 2016; Lanzoni et al., 2017b). This ~~slope was~~ inclination was required to mobilize the dry material solely by gravity and to prevent early deposition before or on the erodible bed. The chosen angle was close to the internal friction angle of the ~~erodible~~ Qtz and Mag beds (Table 1), representing the steepest angle at which these beds remained stable without spontaneous failure. However, due to the comparatively low internal friction angle of Glass, the Glass beds ~~had to be~~ were stabilized with 4–5% water ~~and were uniformly~~ by mass and surficially compacted to increase particle cohesion (Table 1). The selected angle therefore represents a compromise between ensuring sufficient mobility and erosion, initially stable and reproducible bed conditions, and save flume operation. After each experiment, the flume was returned to a horizontal position for post-experimental measurements.

2.3 Instrumentation, measurements, and data processing

Flow height and average flow-front velocity were derived from seven ultrasonic sensors (WayCon UFP-400; 30–400 mm range, 60 ms sampling interval, ±1 mm accuracy) installed normal to the bed along the channel centerline (us1–us7; Fig. 2). The sensors were positioned in systematic intervals to capture both the temporal evolution of the flow at specific locations and its spatial development downslope. ~~To prevent potential data gaps from signal loss, most~~ Most sensors were installed in pairs: us1–us2 at the end of the upper rigid bed, us3 above the transitional bed, us4–us5 above the erodible bed, and us6–us7 at the end of the lower rigid bed. Data recording was synchronized with the reservoir opening, as the sensor trigger was coupled to the flap-release mechanism. Postprocessing of the records was performed in MATLAB® v2023b. For each sensor, flow height was derived by subtracting the mean value of the first-second measurements (representing the initial bed level at flow height 0 cm) from every subsequent data point in the time series. The signals were then smoothed using a moving-average filter over 0.1 s intervals. At the rigid bed sections, the resulting flow height corresponds directly to the actual slide thickness, as the bed surface remained fixed at 0 cm. At the erodible bed, ~~however,~~ ongoing erosion lowered the ~~surface, so records~~ bed surface. The records from us4–us5 therefore represent an apparent flow height that ~~reflects a mixed signal of both~~ combines temporal variations in slide thickness and bed-level change. Flow-height values can thus even become negative when erosion becomes deeper than slide thickness. Flow-front arrival was defined as the moment when the flow height first exceeded a 1 mm threshold. Flow-tail passage was defined as the first time after flow-front arrival that the decreasing flow height crossed the mean height calculated over the last 1.5 s of the ultrasonic record, after the flow had completely passed the sensor. ~~Flow-front~~ Average flow-front velocity was calculated from the ~~ratio of the~~ traveled distance from ~~the~~ reservoir flap to each sensor (Fig. 2a) ~~and the respective timeof~~ divided by the corresponding flow-front arrival time. Cumulative average velocities were preferred over section-wise velocities between adjacent sensors. Over the short inter-sensor distances, small uncertainties in detecting flow-front arrival would strongly affect the calculated section-wise velocities, particularly when individual particles saltated ahead of the flow front.

We also derived an apparent mean erosion rate at sensor us4~~,~~. It was calculated as the ratio between the final ~~erosion depth~~ slope-normal erosion depth inferred from the flow-height record and the duration of ~~debris-flow~~ flow passage at us4. We refer to this rate as "apparent" because it does not capture the temporal variability of the erosion process but represents an average over the entire flow duration at this single location. In reality, however, the flow tail likely exerts insufficient shear stress to sustain erosion and instead promotes material deposition onto the erodible bed (e.g., De Haas et al., 2015)~~, leading~~. This leads to an underestimation of the final erosion depth that reflects the bed surface after ~~tail~~ complete flow-tail passage.

Deposit morphology was mapped using a 3D-surface scanner (MotionCam-3D L Blue LC3R; 2.5 × 2.1 m scan area, 2 Mpx resolution, <1.25 mm accuracy) mounted above the runout area with perpendicular view to the 10°-inclined surface (Fig. 2). The scanner was positioned along the centerline, and x, y, z coordinates were referenced with a marker board fixed to one lateral rim of the scan area. For deposits extending beyond the scan area, the scanner was repositioned downstream by a guide rail system to capture the whole runout area. A second scan overlapping the first at the marker board position was

acquired and merged with the first by exact alignment at the marker board, establishing a shared coordinate system (Fig. 2a,b). Scans were performed with the flume in a horizontal position to prevent signal reflection from the channel outlet, which protruded into the scan cone when the flume was inclined (Fig. 2a). Therefore, the morphologies presented below represent only material deposited on the runout area but do not account for in-channel deposition. Postprocessing of the obtained 3D point clouds was carried out in MATLAB® v2023b. Deposits were first isolated by subtracting a reference scan of the planar, empty runout area. ~~In a subsequent~~ Only the coherent deposit bodies were retained and disconnected particles were excluded, using a cluster analysis based on a minimum Euclidean distance of 5 mm~~, only the coherent deposit bodies were retained and disconnected particles were excluded~~. Finally, the remaining point clouds were converted into 3D-volume models using triangulation-based natural neighbor interpolation with a grid resolution of 3 mm. From the 3D-volume models, geometric and volumetric parameters of the mixed slide–bed deposits on the runout area were determined, including the deposit's length (L), width (W), maximum height, extent ratio (L/W), covered area, volume, center of volume, as well as the travel angle, which is defined here as the inclination between the deposit's center of volume and the lower edge of the reservoir outlet (Fig. 2a). Note that the center of volume should not be interpreted as the center of mass, since the mixed slide–bed deposits can contain materials of varying densities.

The internal structure of the Qtz–Glass and Qtz–Mag deposits on the runout area was examined qualitatively by slicing the deposits laterally into regular cross sections. Each profile was created by inserting a 2 mm thin glass plate vertically into the deposit and capturing the exposed section with a camera, after the material in front of the glass plate had been removed. This qualitative approach was not applied to Qtz–Qtz deposits, as the Qtz bed was not colored to preserve its natural surface properties and ensure identical conditions and material reusability, making particles from slide and bed indistinguishable.

2.4 Experimental reproducibility

To evaluate reproducibility, a total of 24 ~~debris-flow~~ dry granular flow experiments (Exp1–Exp24) were performed, 12 for each ~~material size~~ particle-size fraction. Both ~~fine and coarse~~ fine- and coarse-particle experiments comprised all four scenarios (~~weak, neutral, strong, and~~ low density, equal density, high density, or reference), with every scenario repeated three times. To maintain consistent conditions, all experiments followed the same sequence of preparation and operation steps. The full set of ~~debris-flow~~ dry granular flow experiments is summarized in Table 2 and frontal photographs of all experiments are provided in the Supplement in Figures S1 and S2.

From the three repetitions per scenario, one representative run was selected for detailed presentation and illustration: fine-particle experiments – Glass/f (Exp5), Qtz/f (Exp1), Mag/f (Exp7), reference (Exp12); coarse-particle experiments – Glass/c (Exp18), Qtz/c (Exp14), Mag/c (Exp20), reference (Exp22). The selection is based on the best overall agreement in flow-front arrival time and early-stage flow-height evolution across the four scenarios recorded at sensor us2 (see Sect. 3.1.1). This sensor served as a control for consistent initial flow behavior, as the flow at this location consisted solely of the released Qtz–slide, which was identical in all runs within a particle-size fraction. Unless stated otherwise, the data presented hereafter refer to these representative runs.

Table 2. ~~Experimental debris-flow conditions~~ Conducted dry granular flow experiments as well as measures of the respective deposit ~~characteristics~~on the runout area.

Experiment						Deposit measures						
Exp ID	~~Fraction~~Series	Scenario	Slide	Bed~~(scenario)~~	Rep	Length (cm)	Width (cm)	Height (cm)	Area (m^2)	Volume (L)	~~L/W~~[**]CoV[b] (cm)	Travel ~~angle~~[***]angle[c] (°)
~~Exp1~~[*] Exp1[a]	fine	~~Qtz~~ equal density	Qtz/f	Qtz~~(neutral)~~ /f	1	97	92	22	0.7	53	~~1.0~~ 33	34.2
Exp2	fine	~~Qtz~~ equal density	Qtz/f	Qtz~~(neutral)~~ /f	2	85	94	22	0.7	56	~~0.9~~ 32	34.2
Exp3	fine	~~Qtz~~ equal density	Qtz/f	Qtz~~(neutral)~~ /f	3	85	88	21	0.6	49	~~1.0~~ 31	34.3
Exp4	fine	~~Qtz~~ equal density	Qtz/f	Glass~~(weak)~~ /f	1	157	94	16	1.3	74	~~1.7~~ 64	32.7
~~Exp5~~[*] Exp5[a]	fine	~~Qtz~~ equal density	Qtz/f	Glass~~(weak)~~ /f	2	157	92	15	1.3	75	~~1.7~~ 66	32.5
Exp6	fine	~~Qtz~~ equal density	Qtz/f	Glass~~(weak)~~ /f	3	159	90	15	1.2	68	~~1.8~~ 66	32.5
~~Exp7~~[*] Exp7[a]	fine	~~Qtz~~ high density	Qtz/f	Mag~~(strong)~~ /f	1	90	89	21	0.7	51	~~1.0~~ 34	34.3
Exp8	fine	~~Qtz~~ high density	Qtz/f	Mag~~(strong)~~ /f	2	96	84	19	0.7	48	~~1.1~~ 35	34.3
Exp9	fine	~~Qtz~~ high density	Qtz/f	Mag~~(strong)~~ /f	3	96	85	19	0.7	46	~~1.1~~ 35	34.3
Exp10	fine	~~Qtz~~ reference	Qtz/f	-	1	135	82	16	1.0	60	~~1.6~~ 53	33.5
Exp11	fine	~~Qtz~~ reference	Qtz/f	-	2	140	83	16	1.0	67	~~1.7~~ 56	33.3
~~Exp12~~[*] Exp12[a]	fine	~~Qtz~~ reference	Qtz/f	-	3	146	83	15	1.1	71	~~1.7~~ 59	33.1
Exp13	coarse	~~Qtz~~ equal density	Qtz/c	Qtz~~(neutral)~~ /c	1	127	78	17	0.9	46	~~1.6~~ 47	33.9
~~Exp14~~[*] Exp14[a]	coarse	~~Qtz~~ equal density	Qtz/c	Qtz~~(neutral)~~ /c	2	127	82	18	0.9	49	~~1.5~~ 48	33.9
Exp15	coarse	~~Qtz~~ equal density	Qtz/c	Qtz~~(neutral)~~ /c	3	132	82	18	0.9	51	~~1.6~~ 48	33.9
Exp16	coarse	~~Qtz~~ low density	Qtz/c	Glass~~(weak)~~ /c	1	316	129	11	3.1	91	~~2.1~~ 114	29.2
Exp17	coarse	~~Qtz~~ low density	Qtz/c	Glass~~(weak)~~ /c	2	336	135	10	3.6	91	~~2.5~~ 115	29.1
~~Exp18~~[*] Exp18[a]	coarse	~~Qtz~~ low density	Qtz/c	Glass~~(weak)~~ /c	3	303	125	11	2.9	89	~~2.1~~ 101	30.0
Exp19	coarse	~~Qtz~~ high density	Qtz/c	Mag~~(strong)~~ /c	1	128	83	17	0.9	51	~~1.5~~ 51	33.7
~~Exp20~~[*] Exp20[a]	coarse	~~Qtz~~ high density	Qtz/c	Mag~~(strong)~~ /c	2	129	79	17	0.9	50	~~1.6~~ 49	33.8
Exp21	coarse	~~Qtz~~ high density	Qtz/c	Mag~~(strong)~~ /c	3	121	79	17	0.8	47	~~1.5~~ 47	33.9
~~Exp22~~[*] Exp22[a]	coarse	~~Qtz~~ reference	Qtz/c	-	1	245	114	12	1.9	83	~~2.2~~ 138	27.8
Exp23	coarse	~~Qtz~~ reference	Qtz/c	-	2	242	104	11	1.7	81	~~2.3~~ 137	27.9
Exp24	coarse	~~Qtz~~ reference	Qtz/c	-	3	228	100	13	1.6	81	~~2.3~~ 127	28.6

~~*~~ [a] Runs selected for detailed ~~analysis~~ presentation and illustration in this study (see Sect. 2.4).

~~** Length-to-width ratio~~ [b] Center of volume as longitudinal (downslope) distance.

~~*** Defined as the inclination~~ [c] Inclination between the deposit's center of volume and the lower edge of the reservoir outlet.

~~From the three repetitions per scenario, one representative run was selected for detailed analysis and illustration: fine fraction – Glass/f (Exp5), Qtz/f (Exp1), Mag/f (Exp7), reference (Exp12); coarse fraction – Glass/c (Exp18), Qtz/c (Exp14), Mag/c (Exp20), reference (Exp22). The selection was based on the best overall agreement in~~

3 Results

The results are presented in two parts. The first part describes the spatiotemporal evolution of the dry granular flows in the channel, including flow height, bed erosion, and average flow-front ~~arrival time and early-stage flow-height evolution across the four scenarios recorded at sensor us2 (see Sect. 3.1.1). This sensor served as a control for consistent initial debris-flow behavior for the four scenarios, as the flow at this location consisted solely of the released Qtz–slide, which was identical in all runs within a size fraction. Unless stated otherwise, the data presented hereafter refer to these representative runs~~velocity. The second part analyses the resulting deposits on the runout area, including deposit morphology, and the internal structure of selected mixed slide–bed deposits. Within each subsection, the observations are followed by a brief mechanistic interpretation of the key findings. The discussion then integrates these individual mechanistic interpretations into a broader process-based framework.

4 ~~Results~~

3.1 Spatiotemporal ~~debris-flow~~ flow evolution and bed erosion

The flow-height hydrographs from the ultrasonic sensors illustrate the spatiotemporal evolution of ~~fine and coarse debris-flow passage along the flume~~ the dry granular flows along the channel (Fig. 3). We present below the data from us2, us4, and us6, which capture the key stages of ~~debris-flow~~ flow progression: pre, during, and post erosion. The remaining sensors recorded equivalent trends and are shown in the Supplement ~~to avoid redundancy (Supplement Figs.~~in Figures S3 and S4~~). Flow-height signals were highly reproducible across all repeated fine and coarse experiments~~ , along with the repeated experiments that demonstrate high reproducibility of the flow-height signals.

3.1.1 Flow heights upstream the erodible bed

Before reaching the erodible bed (us2 in Fig. 3), flow heights show a nearly identical temporal evolution across all scenarios. The early Qtz–slides are characterized by a rapid rise and a more gradual subsequent decay in flow height ~~. The timing of~~ with well-defined and consistent flow-front arrival and flow-tail passage~~is well defined and consistent. In the fine experiments,~~ . The fine-particle flow fronts reach us2 about 1.3 s after slide release and the slides pass within 5 s. They thicken up to 5 cm, with peak height occurring near the flow head. ~~In the coarse experiments,~~ The coarse-particle flow fronts arrive at the same time but the slides pass within 4 s. Peak heights remain thinner at 3.5 cm and the association between peak height and flow front is less distinct.

The close agreement among all scenarios within each particle-size fraction at us2 thus confirms comparable initial flow conditions at the entrance to the erodible bed. Differences observed farther downslope can therefore be attributed primarily to subsequent flow–bed interactions rather than to systematic differences in release time or upstream flow conditions.

3.1.2 Flow heights on the erodible bed and local bed erosion

At the erodible bed ~~,~~ (us4 in Fig. 3), flow fronts still arrive almost simultaneously across all scenarios~~. Yet, the temporal evolution of flow heights begins to diverge, the relative tendencies remaining the same in the fine and coarse experiments.~~

~~In the reference experiments without erosion~~, but subsequent flow evolution differs markedly. In the non-erosive reference scenarios, flow evolution at us4 resembles that observed at us2 but with a flatter and more elongated passage. The ~~fine debris~~ fine-particle flow passes within 5.0 s at ~~maximum~~ a maximum thickness of 4 cm~~thickness~~, while the ~~coarse debris~~ coarse-particle flow passes within 4.5 s ~~reaching~~ and reaches a peak height of 3 cm.

In the erosive ~~experiments~~scenarios, by contrast, flow fronts steepen immediately upon arrival, and the duration of ~~debris-flow~~ flow passage increases compared to us2. ~~Fine debris~~ Fine-particle flows pass the sensor in about 7 s, whereas ~~coarse debris~~

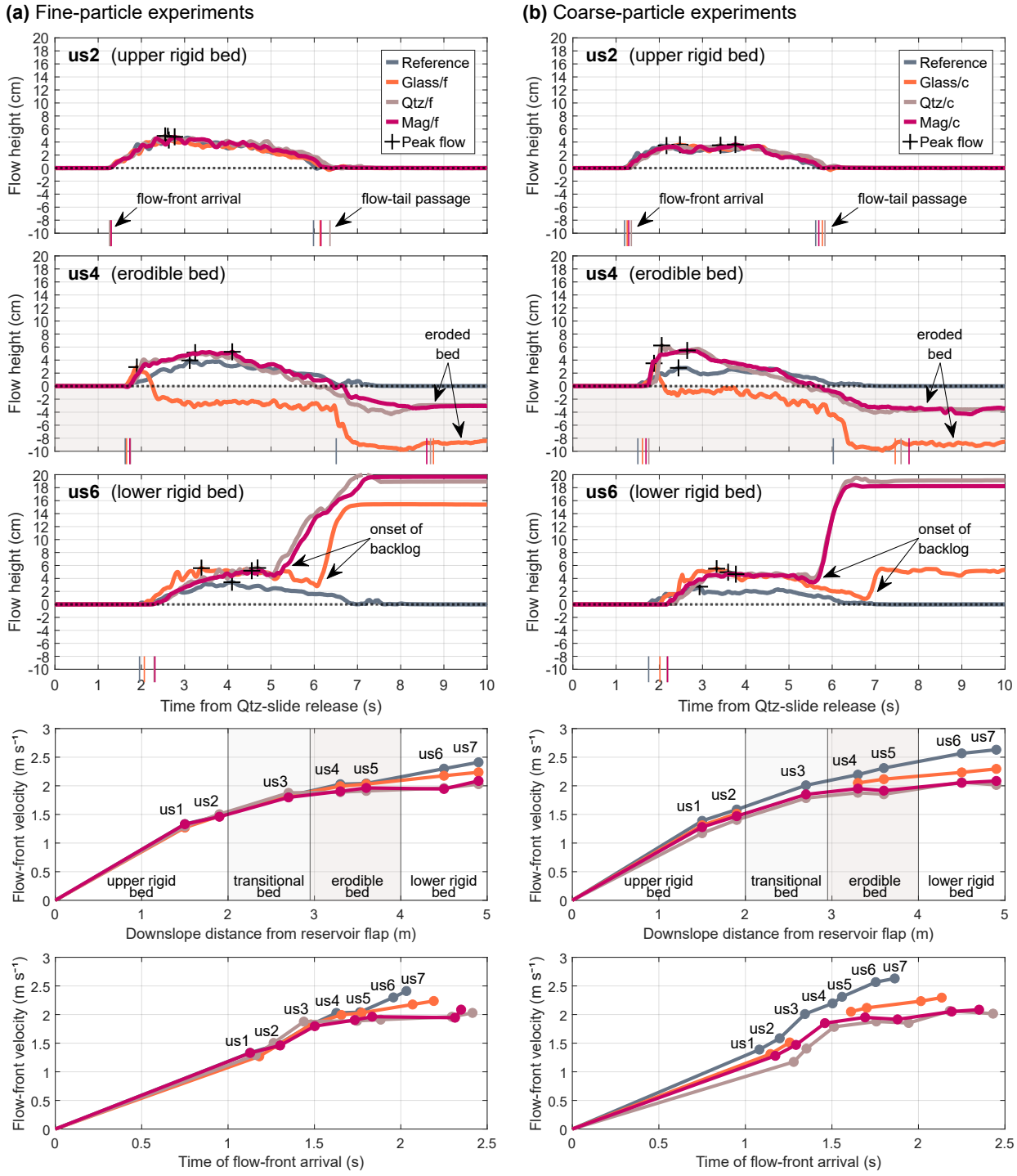


Figure 3. Spatiotemporal ~~debris-flow~~ flow evolution of (a) fine- and (b) coarse-particle experiments. From top to bottom: evolution of flow height over time at us2 (before the erodible bed), us4 (on ~~/eroding~~ the erodible bed), and us6 (before the runout area), as well as average flow-front velocity from reservoir flap to sensor over downslope distance, and over time. Representative runs are shown (see Sect. 2.4). Note that in (b), no data point is shown at us3 for the Glass/c experiment in the two lower panels due to a brief ultrasonic signal loss during flow-front passage. /f: fine particles; /c: coarse particles; us: ultrasonic sensor.

coarse-particle flows pass within 6 s ~~, developing~~ and develop slightly steeper fronts. ~~Yet, the magnitude and manner of bed erosion and surface lowering differ~~

The non-erosive reference scenarios provide the baseline for interpreting the changes observed in the erosive scenarios at us4. Their evolution is consistent with continuous acceleration downslope and longitudinal stretching of the slide over the rigid bed. Over the erodible beds instead, the steeper flow fronts and longer passage durations are consistent with an abrupt increase in basal resistance and with momentum transfer from the moving slide to the initially resting bed. The resulting reduction in average flow-front velocity may cause following material to accumulate behind the flow front and produce local flow-front steepening and thickening. Ongoing entrainment of bed material further prolongs the passage of the mixed flow. The slightly longer passage of the fine-particle flows suggests higher dispersive stresses in a more compact flow body, whereas the coarse-particle flows appear to move in a lower dispersed state with a sharper, faster passing front.

After flow-front passage, the flow heights reveal different erosion behavior among the erosive scenarios at us4. In the Glass experiments, flow-height evolution follows a ~~distinct three-step pattern: a steep , instantaneous~~ stepwise pattern. A steep flow front coincides with ~~peak-flow~~ peak flow height, followed by an abrupt first decline around 2 s after slide release, during which the ~~debris-flow~~ flow surface drops below the original bed level~~, and a~~ . A second, more pronounced decline occurs toward the end of the event, around 6.5 s after slide release. After ~~debris-flow passage, nearly~~ flow passage, the entire 10 cm thick bed is eroded. In the ~~fine~~ fine-particle experiment (Glass/f), the successive drops reach -2.5 and -8.7 cm below the original bed surface, ~~resulting in~~ corresponding to an apparent mean erosion rate of about ~~1.0~~1.2 $\mathrm{cm\,s^{-1}}$. In the ~~coarse~~ coarse-particle experiment (Glass/c), the two successive drops reach about -1.0 and -8.9 cm, ~~yielding~~ corresponding to an apparent mean erosion rate of about ~~1.2~~1.5 $\mathrm{cm\,s^{-1}}$. In the Qtz and Mag experiments, flow heights evolve more gradually and ~~behave almost congruently~~ remain nearly identical for both materials. The ~~debris~~ flows thicken initially toward peak flow and then decrease continuously, falling only slightly below the original bed level. In the ~~fine~~ fine-particle experiments (Qtz/f and Mag/f), flow heights reach an early peak ~~,~~ before declining to final erosion depths of approximately -2.9 and -3.1 cm, corresponding to apparent mean erosion rates of ~~0.3 and~~ 0.4 and 0.5 $\mathrm{cm\,s^{-1}}$, respectively. In the ~~coarse~~ coarse-particle experiments (Qtz/c and Mag/c), peak height occurs earlier and the subsequent decline begins sooner. Final erosion depths ~~of~~ are slightly larger with about -3.6 and -3.7 cm~~correspond~~ , corresponding to apparent mean erosion rates of ~~0.5~~0.6 $\mathrm{cm\,s^{-1}}$.

The contrasting erosion patterns reflect fundamentally different flow–bed interactions at us4. In the Glass experiments, the initial drop in flow height suggests rapid erosion of the upper Glass bed. Due to the low solid particle density of Glass, the Qtz-slide transfers less momentum to accelerate a given eroded bed volume than it would for a denser bed, resulting in comparatively limited momentum loss within the moving flow. In addition, the rounded particle shape reduces grain interlocking and internal frictional resistance, providing only limited resistance against the erosive shear exerted by the denser Qtz-slide. The stepwise lowering may reflect localized impact-induced ploughing (Zhang et al., 2026), although the underlying mechanism cannot be resolved from the present measurements. By contrast, the gradual and nearly identical lowering of the Qtz and Mag beds indicates higher resistance against erosion and entrainment. For a given eroded bed volume, the Qtz-slide has to transfer more momentum to accelerate the denser Qtz or Mag. This effect is likely reinforced by their angular particle

shape, which promotes grain interlocking and internal frictional resistance. Yet, the close agreement between the lighter Qtz and heavier Mag indicates that the higher solid particle density of Mag did not produce a distinct erosion signal at us4.

3.1.3 Flow heights downstream the erodible bed

After erosion and before depositing on the runout area (us6 in Fig. 3), the timing of flow-front arrival ~~appears to differ~~ differs among the four scenarios ~~,~~ by a few tenths of a second. The ~~references arrive first~~ non-erosive reference flows arrive first at, followed by Glass, while Qtz and Mag reach ~~the sensor~~ us6 last and simultaneously. ~~Fine debris~~ The fine-particle flows arrive a few milliseconds later than ~~coarse debris flows. It is noted that flow heights in the erosive experiments~~ the coarse-particle flows.

The morphologic changes that developed on the erodible bed were thus propagated downstream and are reflected in the flow-front arrival times at us6 and before the runout area. In the erosive scenarios, flow heights show a distinct late rise ~~, whereas the reference experiments display none~~that is absent in the non-erosive reference scenarios. This late rise results from the ~~debris~~ flow backing up into the channel instead of being fully released onto the runout area, leading to in-channel deposition. ~~The resulting~~ This backlog obscures the timing of the flow tail and is more pronounced for ~~fine debris~~ fine-particle flows, which develop an earlier and stronger material accumulation than ~~coarse debris~~ coarse-particle flows.

3.1.4 ~~Flow-front~~ Average flow-front velocities~~downslope~~

~~Flow-front velocities overall increase with distance downslope , showing a steep initial rise that gradually tapers off in both fine and coarse~~ Average flow-front velocities from reservoir flap to each sensor overall increase downslope in both fine- and coarse-particle experiments (Fig. 3). ~~Velocities increase consistently~~ As expected for gravity-driven acceleration from rest, velocities increase steeply along the upper rigid bed, reaching about 1.5 $\mathrm{m\,s^{-1}}$ at us2. On the erodible bed at us4, velocity trends begin to diverge among the four scenarios. In the ~~reference experiments, velocities continue to increase approximately linearly downslope~~non-erosive reference scenarios, flow fronts continue to accelerate nearly constantly, reaching the highest final ~~values~~ velocities of about 2.4 $\mathrm{m\,s^{-1}}$ in the ~~fine~~ fine- and 2.6 $\mathrm{m\,s^{-1}}$ in the ~~coarse debris flow~~coarse-particle flows. In the erosive scenarios, acceleration begins to decrease once the Qtz–slides encounter the erodible bed. In the Glass experiments, ~~flow-front velocities also increase~~ flow fronts continue to accelerate along the erodible bed~~but~~ , although with a slightly reduced gradient. Both ~~fine and coarse debris~~ fine- and coarse-particle flows reach about 2.2 $\mathrm{m\,s^{-1}}$ at us7, shortly before deposition. In the Qtz and Mag experiments, ~~velocities remain nearly constant once the debris flows encounter~~ the flows no longer accelerate once encountering the erodible bed ~~, with fine and coarse debris flows maintaining values around~~ and the velocities of both fine- and coarse-particle flows remain nearly constantly at 2.0 $\mathrm{m\,s^{-1}}$ ~~before the runout~~ until reaching the runout area.

~~The time-dependent evolution of~~ The evolution of average flow-front velocities ~~, indicating flow-front acceleration, is likewise distinct (Fig. 3). In the reference experiments, the flow fronts accelerate nearly constantly over time, with the coarse debris flow showing a distinctly steeper increase than the fine debris flow. In the erosive experiments, acceleration is initially similar to the~~

~~reference experiments but begins to decrease once the Qtz–slides encounter the erodible bed. This decline is less pronounced for Glass but clearly visible for~~ is consistent with the erosion behavior observed in the flow-height records at us4 (see Sect. 3.1.2). The continued, although reduced, acceleration over the Glass beds is the minor consequence of enhanced erosion and basal friction. By contrast, the velocity plateau over the Qtz and Mag beds is consistent with the more gradual bed lowering observed at us4, where the ~~debris flows no longer accelerate after passing the erodible bed~~ larger momentum transfer required to erode and accelerate denser bed material counteracts further downslope acceleration.

3.2 Runout characteristics

The 3D surface scans and lateral cross sections of the final deposits characterize deposition in the runout area and provide additional information on transport and entrainment processes in the channel. We first present the deposit geometry and runout metrics for all scenarios, and then describe the internal material distribution of the mixed Qtz–Glass and Qtz–Mag deposits.

3.2.1 Deposit morphology

The deposits are largely symmetric along the central downslope axis. Deposit geometries differ ~~clearly~~ among the four scenarios and consistently in both ~~size~~ particle-size fractions (Figs. 4 and 5). ~~All deposits are largely symmetric along the central downslope axis. Yet, most deposits show an artificial drop in height toward the channel outlet at $(0|0)$, due to partial material loss when the flume was leveled for surface scanning (see Sect. 2.3 and Supplement Fig. S5). This artifact, however, does not affect the overall depositional pattern. Below, the four scenarios for both size fractions are summarized. All~~ The repeated runs yielded highly consistent deposit morphologies, resulting in comparable metrics (Table 2) and near-congruent shapes (Table 5) across the three repetitions (~~Table 2, Fig. 5;~~ see Supplement Figs. S6 and S7 for all deposit contour plots). Runout lengths vary by less than $\pm 4\%$ from the mean of the three repeated runs for most scenarios and by a maximum of ~8% (Supplement Table S1). Note, however that the deposit topographies show an artificial slope toward the channel outlet at $(0|0)$. This drop in thickness results from lowering the flume into the horizontal position after the experiment (see Sect. 2.3 and Supplement Fig. S5). The rear part of the deposit adjusts then to the sediment-specific angle of repose, causing a small amount of material to slide backward out of the runout area before scanning. This artifact, however, does not affect the overall depositional pattern.

~~Deposit geometry and experimental reproducibility for (a) fine- and (b) coarse-particle experiments. From top to bottom: deposit outlines, downslope runout height along the central deposit line, as well as travel angle and L/W for all repetitions. Bold lines and filled symbols indicate the representative runs (see Sect. 2.4); thin lines or open symbols show their repetitions. /f: fine particles; /c: coarse particles; L/W: length-to-width ratio.~~

~~The reference experiments~~ The non-erosive reference deposits form elongated, well-confined lobes. The ~~fine~~ fine-particle deposit ($L/W \approx 1.7$; Figs. 4a and 5a) tapers gradually downslope, reaching a runout length of 146 cm and covering an area of 1.1 m^2 with a volume of 71 L. The ~~coarse~~ coarse-particle deposit ($L/W \approx 2.2$; Figs. 4b and 5b) is isolated on the runout area,

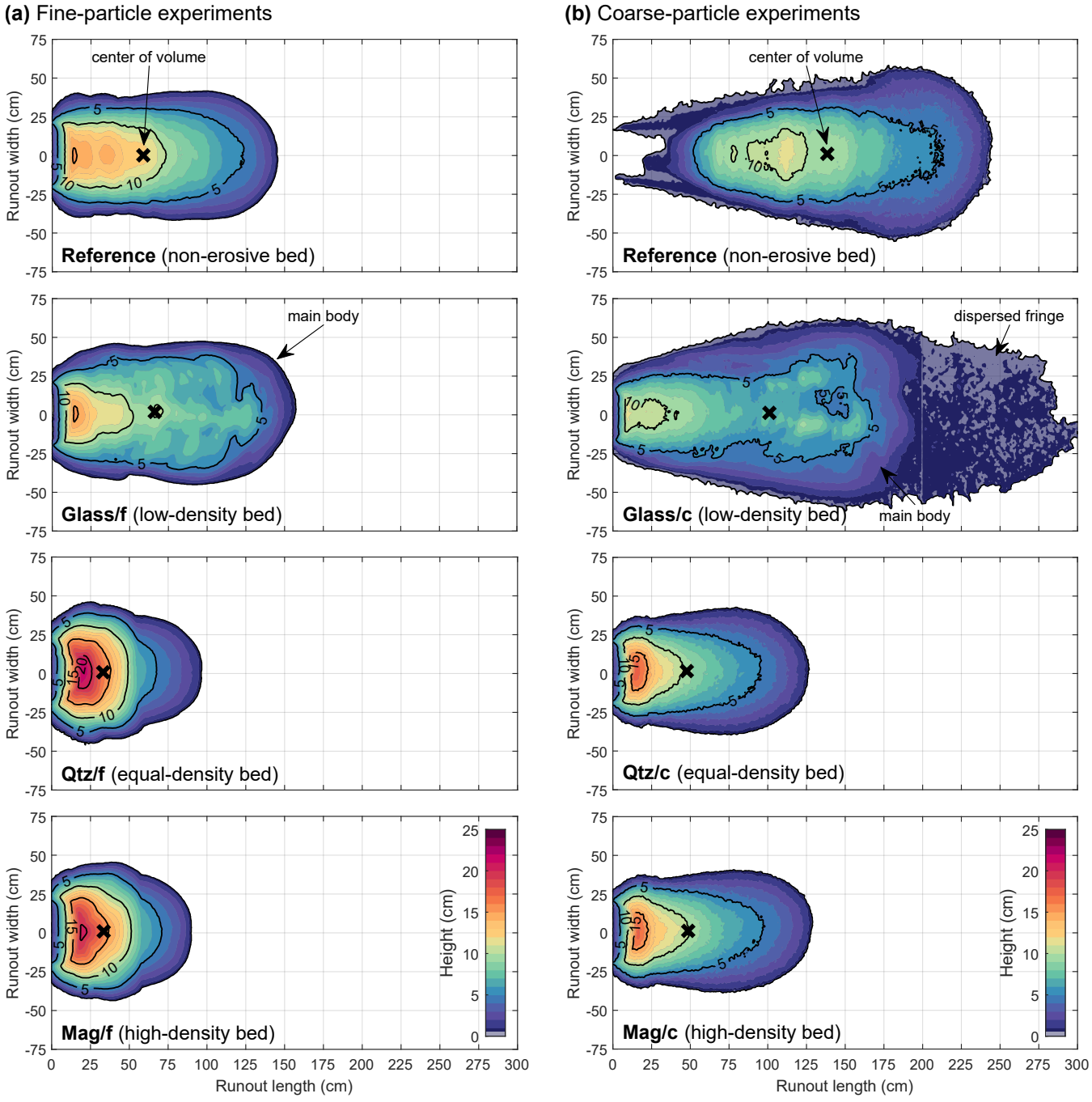


Figure 4. Deposit morphology of (a) fine- and (b) coarse-particle experiments. From top to bottom: contours of deposit height for the non-erosive reference~~case without erosion~~, the glass bed, the quartz bed, and the magnetite bed. Representative runs are shown (see Sect. 2.4). Note that the flume was repositioned to the horizontal before deposit scanning~~; therefore~~. Therefore, only material deposited beyond the flume outlet was analyzed, and the apparent thickness drop towards $(0|0)$ is a systematic artifact (see Supplement Fig. S5). /f: fine particles; /c: coarse particles.

as all material was released from the channel, extending to a maximum runout of 245 cm, an area of 1.9 m^2, and a volume of 83 L. In both ~~size~~ particle-size fractions, the centers of volume are located near the top-view midpoint of the deposit.

~~The Glass experiments produce~~

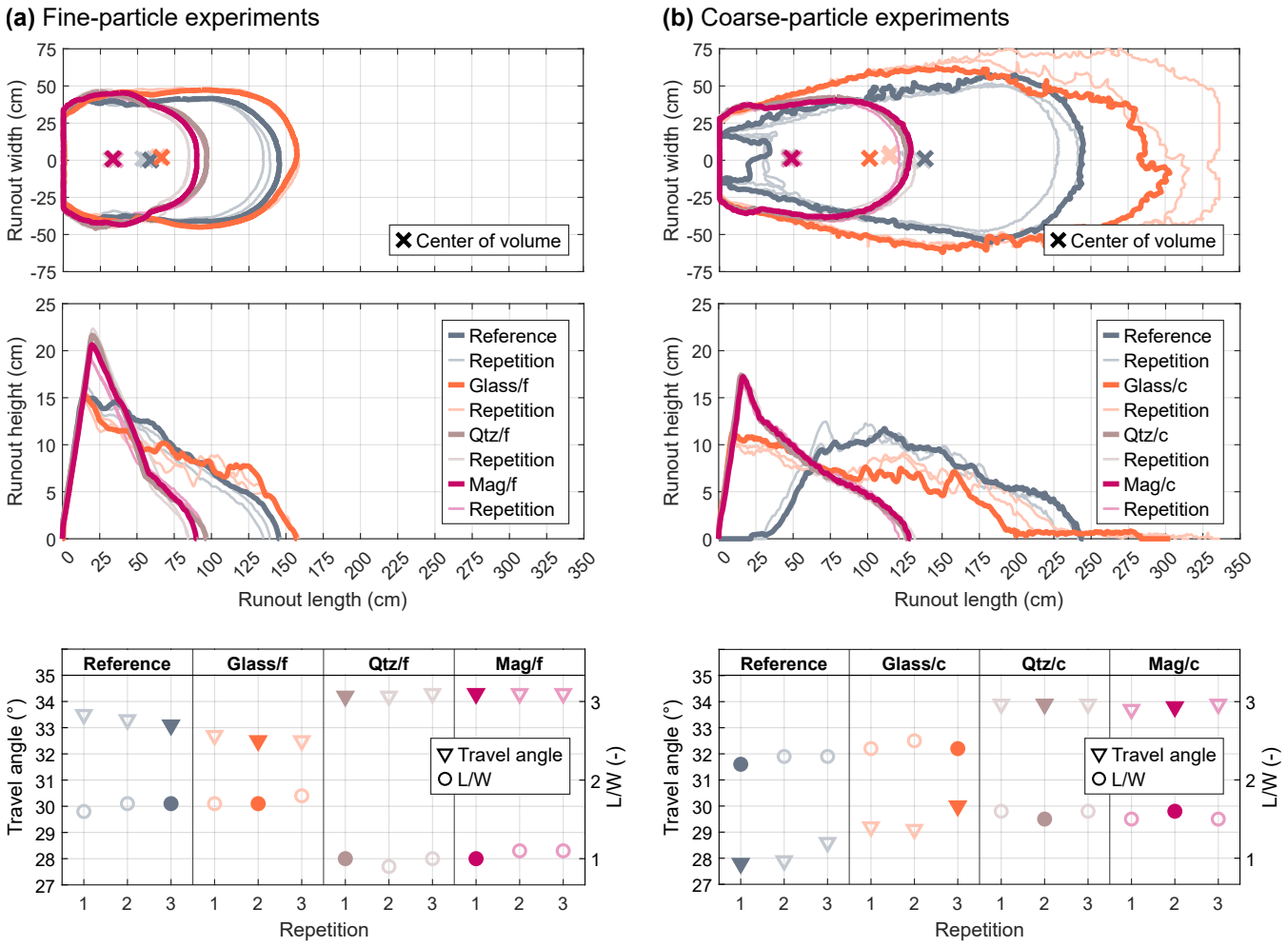


Figure 5. Deposit geometry and experimental reproducibility for (a) fine- and (b) coarse-particle experiments. From top to bottom: deposit outlines, downslope runout height along the central deposit line, as well as travel angle and L/W for all repetitions. Bold lines and filled symbols indicate the representative runs (see Sect. 2.4); thin lines or open symbols show their repetitions. /f: fine particles; /c: coarse particles; L/W: length-to-width ratio.

The Glass deposits form elongated lobes with undulating surfaces, but their shape differs markedly ~~between the fine and coarse debris flow. The fine~~ for the two particle-size fractions. The fine-particle deposit (Glass/f; Figs. 4a and 5a) forms a well-confined lobe ($L/W \approx 1.7$) with clear lateral margins and decreases gradually in height downslope. ~~It's~~ Runout length of 157 cm, area of 1.3 m^2, and volume of 75 L resemble the ~~fine reference experiment~~corresponding non-erosive reference deposit. The center of volume lies near the plan-view midpoint. The ~~coarse~~ coarse-particle deposit (Glass/c; Figs. 4b and 5b) is distinctly more

stretched ($L/W \approx 2.4$) reaching with 303 cm almost twice the length and covering with 2.9 m^2 an area roughly double in size. The volume of 89 L is only by <20% larger. The deposit consists of two parts: a compact main body extending over the first 2 m, gradually decreasing in height, and a 1 m long, flat ($\leq$ 1 cm) frontal fringe composed of loosely dispersed particles. The center of volume is located approximately halfway along the main body.

The Qtz and Mag ~~experiments yield almost identical deposit~~ deposits show almost identical shapes and contour patterns within each ~~size~~ particle-size fraction. The ~~fine~~ fine-particle deposits (Qtz/f and Mag/f; Figs. 4a and 5a) are compact ~~, with~~ and runout lengths and widths ~~being~~ nearly equal ($L/W \approx 1.0$). Along the centerline, runout height shows an initial steep decrease that transitions to a gentler gradient beyond a distinct break in slope (at ~55 cm length). Runout lengths are short with 90–97 cm, and cover a small area of 0.7 m^2 with volumes of ~52 L. The ~~coarse~~ coarse-particle deposits (Qtz/c and Mag/c; Figs. 4b and 5b) are more elongated ($L/W \approx 1.5$) and show two breaks in slope in their downslope height profiles (at ~25 and 75 cm length). Their runouts are both nearly 130 cm long, covering an area of 0.9 m^2 and a volume of ~50 L. In both ~~size~~ particle-size fractions, the centers of volume remain close to the channel outlet.

The final runout morphology reflects the material-dependent flow and erosion patterns already observed in the channel. Whereas the non-erosive reference deposits reflect only the spreading and deceleration of the initially released Qtz-slide on the runout area, the mixed slide–bed deposits additionally record the effects of bed erosion and entrainment. The Glass deposits exhibit enhanced longitudinal spreading, with runout length and area increasing disproportionately relative to deposit volume, indicating more efficient spreading of the Qtz–Glass mixture across the runout area. In contrast, the Qtz and Mag deposits remain compact and proximal, mirroring their nearly identical erosion behavior and average flow-front velocities and indicating stronger deceleration during erosion and deposition. Despite its substantially higher solid particle density, Mag produces deposits that are nearly indistinguishable from those of Qtz, indicating that the higher solid particle density of Mag did not translate into a distinct deposit morphology under the tested conditions.

3.2.2 Internal deposit structure

Lateral cross sections through the mixed Qtz–Glass and Qtz–Mag deposits reveal distinct internal sorting and spatial patterns in both ~~fine (Supplement~~ coarse- (Fig. ~~S8) and coarse experiments (~~6) and fine-particle experiments (Supplement Fig. ~~6~~S8). The mixed slide–bed deposits show a finer-grained core that coarsens toward the deposit surface (cross-checks of the Qtz–Qtz and reference deposits confirmed comparable sorting). The sorting is particularly evident in the ~~coarse~~ coarse-particle experiments, where the particle-size spectrum is wider. ~~The material distribution, however, differs between the bed materials~~

This vertical coarsening is consistent with well-known grain-size segregation in dense granular flows, where smaller particles percolate downward through voids while larger particles are displaced upward by kinetic sieving and squeeze expulsion (e.g., Savage and Lun, 1988; Gray and Thornton, 2005; Gray, 2018). In geophysical mass flows, such vertical segregation can be coupled to preferential transport of coarse particles toward the flow surface, front, and margins, thereby influencing deposit architecture and levee formation (e.g., Johnson et al., 2012; Gray, 2018; Baselt et al., 2022).

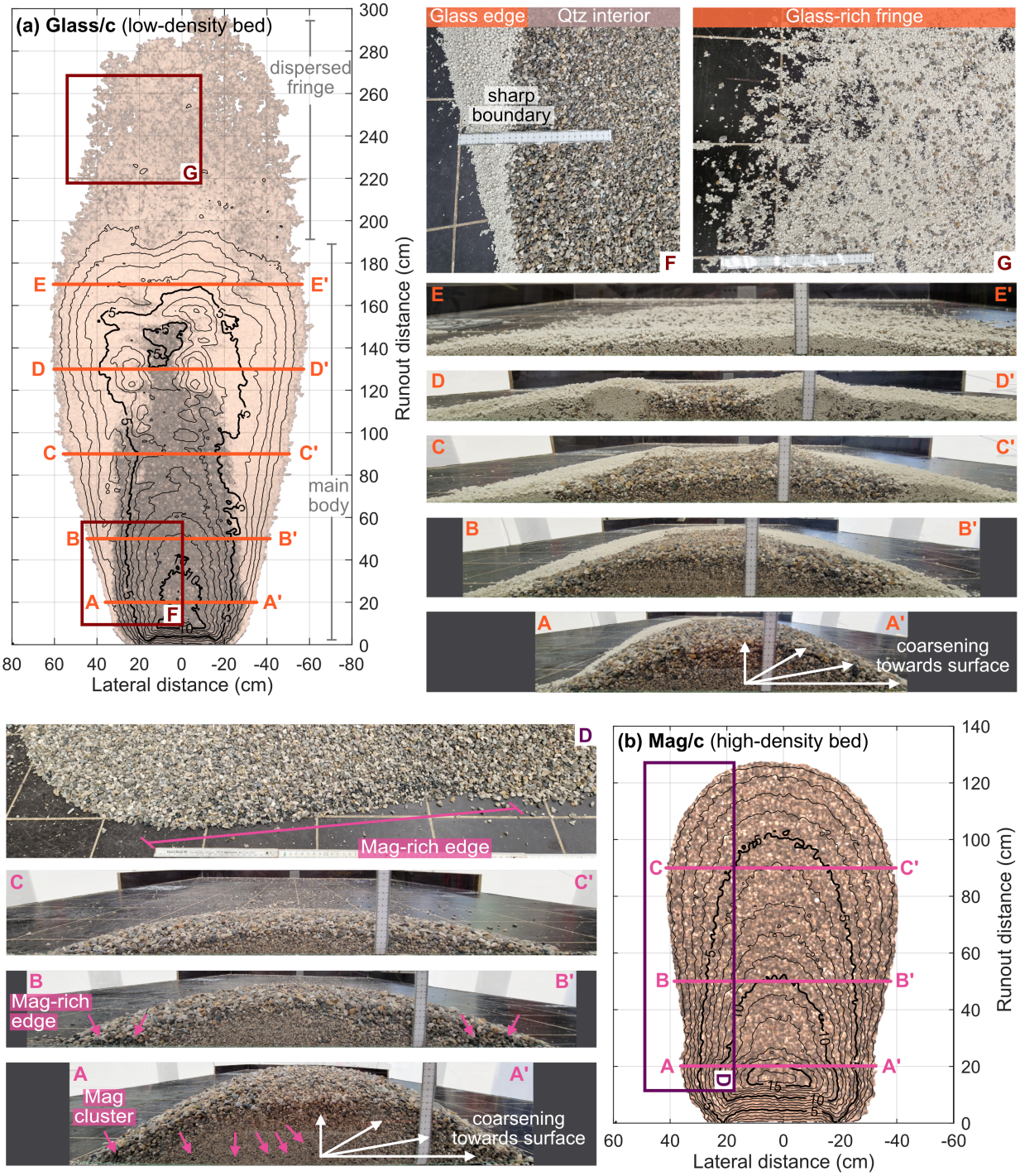


Figure 6. Internal structure and spatial distribution of ~~a~~ the (a) Qtz–Glass and (b) Qtz–Mag deposit from coarse-particle experiments. Positions of lateral cross sections and surface views are indicated on the contoured surface scan. Contour lines are spaced at 1 cm intervals. Note that thicknesses in the cross sections may appear slightly reduced compared to the corresponding contour-plot position, as inserting the glass plate for vertical cutting could drag material downward at the front. Photographs are from Exp18 (Glass/c) and Exp19 (Mag/c).

In the Glass experiments Beyond this general grain-size sorting, the cross sections also reveal material-specific patterns related to the contrasting beds. In the Qtz–Glass deposits (Fig. 6a and Supplement Fig. S8a), a sharp boundary occurs between the two materials. Qtz–slide Qtz particles are concentrated in the interior of the main body, while Glass-bed Glass particles form the lateral edges. With increasing runout distance, the lateral Glass edges widen and the central Qtz core narrows. In the intermediate sections, Glass particles appear laterally shouldered onto a thin Qtz layer and the central Qtz core becomes disrupted by distinct Glass ridges. Toward the distal end of the main bodyfront, the deposits consist almost entirely of Glass. In the fine fine-particle deposit (Glass/f; Supplement Fig. S8a), Glass also appears centrally along the deposit base. In the coarse coarse-particle deposit (Glass/c; Fig. 6a), the frontal meter consists of a fringe mainly composed of loosely dispersed coarse Glass with only a few Qtz particles.

In the Mag experiments In the Qtz–Mag deposits (Figs. 6b and Supplement Fig. S8b), material separation is less distinct due to the similar material colorsvisible and distinct. The deposits appear to be dominated by Qtz–slide Qtz particles, whereas Mag-bed Mag particles occur rather as localized clusters. In the fine fine-particle deposit (Mag/f; Supplement Fig. S8b), Mag particles are concentrated at the edges and within thin basal layers. In the coarse coarse-particle deposit (Mag/c; Fig. 6b), Mag particles form lateral lenses and individual cluster along the deposit base and become largely absent toward the deposit front.

The contrasting material distributions suggest density- and shape-controlled material segregation during runout and deposition. In the Qtz–Glass deposits, the rounded Glass particles were more readily displaced within the mixture as they were less interlocked than the angular Qtz particles and required less momentum transfer to remain mobile. As a result, they could be lifted and transported laterally downslope, whereas the denser and angular Qtz particles came to rest earlier. In the Qtz–Mag deposits, Mag particles were entrained only locally and neither excavated nor transported as efficiently as the ligther Glass. The higher solid particle density required greater momentum transfer for acceleration, and the angular particle shape promoted interlocking and basal retention. Consequently, entrained Mag particles remained in proximal, small basal clusters.

4 Discussion

Following the inertia-based mobility concept of , our experiments span three energy regimes arising from density differences between an initial Qtz–slide and a low-density Glass bed (inertially weak scenario), an equal-density Qtz bed (inertially neutral scenario), and a high-density Mag bed (inertially strong scenario). Reference experiments conducted over a rigid bed provide a baseline for debris-flow behavior without erosion. Across these four scenarios , the data vary systematically, with

Across the four scenarios (low density, equal density, high density, or reference), the dry granular flow experiments reveal distinct material-dependent patterns of erosion, flow evolution, and deposit geometry. The clearest contrast occurs between the Glass beds and the similarly behaving Qtz and Mag beds, and is consistent across both particle-size fractions. The close agreement between repeated runs (Supplement Figs.S1–S4 S1–S4, S6, S7) , supporting supports the use of a single representative run per scenario and demonstrating demonstrates the reproducibility of the trends underlying the flow–bed interactions discussed below.

4.1 ~~Flow–bed inertia~~ Material controls on erosion, entrainment, and ~~its expression in debris-flow~~ mobility~~and runout~~

~~Distinct material-dependent patterns are consistently expressed in both the spatiotemporal debris-flow evolution (Sect. 3.1) and the resulting deposit geometry (Sect. 3.2). Particularly clear contrasts emerge when comparing the inertially weak and inertially neutral scenarios~~

The observed mobility and runout patterns reflect several coupled material and process controls. Because solid particle density was the primary design variable, we first evaluate its contribution before considering bed internal friction, particle shape, bed preparation, segregation, effective entrainment, and particle-size effects.

4.1.1 Solid particle density and flow-volume growth

The clearest experimental contrast occurs between the low- and equal-density scenarios and is reflected in both particle-size fractions. On the low-density Glass beds, ~~greater erosion depths~~ deeper erosion and higher apparent mean erosion rates ~~are accompanied by increasing~~ coincide with continued increases in average flow-front ~~velocities~~velocity, whereas erosion on the equal-density Qtz beds is ~~less pronounced and~~ shallower and average flow-front velocities remain nearly constant once erosion begins (Fig. 3). ~~This contrast indicates greater entrainment and higher mobility for the low-density Glass bed, when compared to neutral conditions. Consistent with this behavior,~~ These observations indicate a more mobile response over the Glass beds and suggest more effective bed mobilization. The same contrast is expressed in deposit geometry. The main bodies of the Qtz–Glass deposits are approximately 1.6 times longer ~~than the Qtz–Qtz deposits~~ and cover nearly twice the area ~~when only considering the main deposit body in both size fractions (Fig. 4). In the case of Glass/c, including the~~ of the corresponding Qtz–Qtz deposits. Including the dispersed frontal fringe~~increases total runout even to~~ , Glass/c reaches even more than twice ~~that~~ the runout of Qtz/c and ~~expands the covered area by more than a factor of three . The internal Qtz–Glass-deposit structures further reflect the strong density contrast in the inertially weak scenarios, with the light Glass particles preferentially transported toward the fronts and lateral edges, while Qtz particles form dense central cores. For Glass/c, this phase separation is particularly evident as dispersed, Glass-dominated fringe ahead of the main deposit body (Fig. 6a). Strikingly, the inertially strong scenarios do not exhibit a systematic reduction in mobility relative to the inertially neutral scenarios. Instead~~covers more than three times the area (Fig. 4). The greater Glass runout may partly reflect the larger volume of mobilized bed material. The associated flow-volume growth may increase flow depth and modify longitudinal pressure gradients during spreading, contributing to runout independently of any direct density-related effect (e.g., Mangeney et al., 2007, 2010). Within mass- and momentum-conserving entrainment frameworks, bed bulk density determines the mass added for a given eroded volume, while the resulting momentum exchange also depends on bed resistance and on how mobilized material is accelerated and incorporated into the flow (Iverson, 2012). Solid particle density is thus mechanically relevant, but its expression in mobility cannot be isolated from the associated erosion volume and flow–bed interaction. By contrast, the equal- and high-density scenarios behave nearly identical. On the equal-density Qtz and high-density Mag beds, erosion, average flow-front ~~velocity and deposit characteristics are fairly congruent between the Mag and Qtz beds. The internal~~

~~Qtz–Mag-deposit structures indicate only limited incorporation of the heavy Mag particles. The deposits are dominated by Qtz–slide particles, while Mag-bed particles occur only as sparse clusters or thin lateral lenses (Fig. 6b). Finally, consistent with the expectation by , our experiments show enhanced mobilityand extended runout when the debris flows entrain material from the~~ velocities, and deposit geometries are comparable despite an almost twofold difference in solid particle density (Figs. 3–5; Table 1).

This asymmetric response only partly agrees with previous findings. The enhanced mobility, deeper erosion, and longer runout observed for the low-density ~~beds in the inertially weak scenarios, relative to the inertially neutral scenarios. However, the entrainment of significantly denser bed materialdoes not result in the anticipated mobility reduction in the inertially strong scenarios under the experimental conditionsconsidered here~~Glass beds are consistent with the experiments of Farin et al. (2014). They found that dry granular flows became more mobile, traveled farther, and eroded more deeply as bed porosity increased and, consequently, bulk density decreased. Likewise, the enhanced mobility over Glass is also qualitatively consistent with the mobility increase proposed by Pudasaini and Krautblatter (2021) for entrainment of mechanically weaker bed material. However, the absence of a corresponding mobility reduction over the high-density Mag beds shows that solid-particle-density contrast does not map uniquely or monotonically onto mobility under the tested conditions. Instead, ~~both equal- and high-density beds lead to comparable deceleration of the debris flow, suggesting similar and higher energy consumption and momentum loss during bed~~ the results support a broader interpretation in which erosion-induced mobility reflects coupled effects of flow-volume growth, bed resistance, bed deformation, and entrainment efficiency (e.g., Iverson, 2012; Farin et al., 2014; Zhang et al., 2026).

4.1.2 Bed internal friction and stability

Among the accompanying material properties, bed internal friction provides the most plausible explanation for the contrasting erosion and entrainment ~~compared to the low-density material. Consequently, when considering only externally observable flow and deposit characteristics, and not intrinsic process dynamics, our results based on density contrasts alone do not provide sufficient support for the inertia-based mobility hypothesis proposed by~~ patterns. The internal friction angles of Glass are 29–31° and substantially lower than the 37° flume inclination (Table 1). Glass beds consequently required stabilization with 4–5% water by mass and slight surficial compaction to remain initially stable. Once disturbed by the overriding flow, their comparatively low frictional resistance facilitated bed deformation and particle mobilization. Also bed failure facilitated volume growth and mobility. By contrast, the internal friction angles of Qtz and Mag span 35–39° and are close to the flume inclination. Their similar and higher internal friction angles are consistent with their comparable resistance to erosion despite their contrasting solid particle densities. Previous granular-flow experiments likewise show that the influence of erosion on mobility depends strongly on bed friction and slope relative to the material's stability threshold (Mangeney et al., 2010).

The ~~presence of an erodible bed noticeably alters debris-flow evolution. Flow fronts steepen immediately upon arrival at the erodible bed, as the basal roughness abruptly increases compared to the rigid plywood surface, decelerating the flow. The erosive scenarios therefore consistently exhibit~~ travel angles provide a complementary bulk measure of this contrasting

resistance. They are systematically lower for the Glass beds than for Qtz and Mag beds (Table 2, Fig. 5). Particularly in the coarse-particle experiments, Glass/c yields values of 29–30° compared with approximately 34° for Qtz/c and Mag/c. Although the travel angle integrates several processes and should not be interpreted as a direct measurement of basal friction, the lower Glass values are consistent with lower apparent resistance and greater mobility during runout (e.g., Parez and Aharonov, 2015; Taylor-Noonan et al., 2022).

Compared to the non-erosive reference scenario, the erosive scenarios show reduced frontal acceleration and lower average flow-front velocities ~~compared to the reference scenarios without erosion, beyond local bed-surface lowering~~ after entering the erodible bed (Fig. 3). ~~This behavior~~ Under the dry conditions considered in this study, this response is consistent with ~~previous flume studies showing that erosion increases flow resistance since part of the available energy is consumed by entrainment processes . In our experiments, this additional energy dissipation during erosion leads to shorter runouts, except in the inertially weak scenarios where the lengths of the main deposit bodies are comparable to the reference scenarios~~ additional resistance associated with bed deformation and the acceleration of initially resting bed material (e.g., Tian et al., 2014; Li et al., 2022). However, erosion does not necessarily reduce mobility. Entrainment from mechanically weakened or saturated beds can instead promote flow acceleration and momentum growth (Iverson et al., 2011). In the present experiments, the additional resistance is reflected in the shorter Qtz and Mag deposits, whereas the main bodies of the Glass deposits attain lengths comparable to those of the non-erosive reference (Fig. 4).

~~Distinct~~ Contrasting erosion and entrainment modes are evident from the temporal ~~evolution of flow heights over the erodible beds (Fig. 3). Whereas the Glass beds are eroded rapidly in a stepwise manner,~~ flow-height records. The stepwise lowering of the Glass beds is consistent with episodic bed failure, whereas the gradual Qtz and Mag ~~beds exhibit more progressive grain-by-grain entrainment.These entrainment mechanisms were identified before by using colored erodible beds, where entrainment through~~ signals are more consistent with progressive shear-driven erosion (Fig. 3). Similar contrasts between localized en-masse ~~failure was inferred from the deposition of largely intact color layers, in contrast to~~ mobilization and progressive grain-by-grain entrainment ~~associated with more homogeneous color mixing. further showed that beds with a water content close to saturation tend to fail en-masse when overridden by debris flows. The similarity to the stepwise erosion observed in our inertially weak scenarios suggests that mechanically weak ground may exhibit comparable entrainment behavior, regardless of whether the weakness arises from high water content or low material density. Eventually, our apparent~~ have been reported in previous flume experiments (De Haas and Van Woerkom, 2016; Roelofs et al., 2023; Zhang et al., 2026). The Glass response therefore points to comparatively low effective bed resistance, arising primarily from low internal friction and, possibly, low solid particle density.

Apparent mean erosion rates span ~~0.3~~0.4–1~~.2~~.5 $\mathrm{cm\,s^{-1}}$ (Table 2). These values overlap with the lower end of erosion rates reported from debris-flow flume experiments over partially saturated beds, including 0.3–1.8 $\mathrm{cm\,s^{-1}}$ reported by Zheng et al. (2021), but remain below the higher experimental ranges (e.g., 5–10 $\mathrm{cm\,s^{-1}}$ in Iverson et al. (2011) and Reid et al. (2011); 1.9–4.3 $\mathrm{cm\,s^{-1}}$ in Li et al. (2018)). They ~~also compare well~~ are also substantially lower than the average erosion rates of 42–54 $\mathrm{cm\,s^{-1}}$ observed in dry granular flow experiments (Barbolini et al., 2005). In comparison with field observations, ~~where~~

our rate estimates fall within the range of average entrainment rates reported for natural debris-flow events ~~entrain at average rates of 1.1–14 over saturated beds and~~ at Chalk Cliffs, Colorado, USA, which are 0.2–0.5 $\mathrm{cm\,s^{-1}}$ over ~~dry~~ dry beds and 1.1–14 $\mathrm{cm\,s^{-1}}$ over saturated beds (McCoy et al., 2012).

~~Fine and coarse experiments exhibit consistent patterns across the different inertial scenarios. Grain-size segregation is evident from all experiments, with coarse particles preferentially accumulated toward the deposit front and surface (Fig. 6), consistent to previous~~ They are, however, well below the maximum local erosion rates of up to 80 $\mathrm{cm\,s^{-1}}$ measured during debris-flow ~~experiments . This sorting may arise from a recirculation mechanism during flow. Whereas finer particles may segregate downward into the flow interior, coarse particles may progressively migrate upward by shear-induced segregation toward the faster-moving surface and be transported forward toward the flow front, where they can recirculate while being continuously advected toward the flow edges. As result, deposition fronts, surfaces, and lateral edges may become enriched in coarse particles . Within a given scenario, final erosion depths, apparent mean erosion rates , and flow-front velocities vary only marginally between both size fractions (Fig. 3). Erosion is slightly deeper and~~ events at Illgraben, Switzerland (Berger et al., 2011). Our apparent mean erosion rates ~~are slightly higher for the coarse experiments, which may reflect variations in bed packing. Coarser beds are typically more loosely packed, facilitating particle mobilization and erosion, while finer beds tend to be more densely packed and mechanically interlocked, which increases their resistance to particle entrainment under otherwise comparable flow conditions. Coarse debris flows pass the ultrasonic sensor stations slightly faster. This difference, however, is likely because releasing the same initial mass as Qtz–slide corresponds to a release volume that is approximately 10 smaller for the coarser fraction due to its higher dry bulk density (Table 1). Despite these comparatively subtle differences in flow dynamics, the final deposit morphology markedly differs between both size fractions. Coarse experiments systematically produce longer, flatter, elongated lobes, whereas fine experiments yield shorter, thicker deposits (Figs. 4 and 5). In the inertially weak scenario, the coarse Qtz–Glass deposit additionally shows a more diffusive margin but remains more compact and laterally confined in the fine case. Yet, volumes on the runout area of fine and coarse deposits are similar, and even identical in the neutral and strong scenarios (Table 2). This decoupling between similar debris-flow dynamics during erosion and contrasting depositional geometries suggests that grain-size-dependent differences in basal friction further influence debris-flow mobility. In the erosive scenarios, fine and coarse debris flows exhibit similar surface and bulk flow behavior while traversing the erodible bed, the underlying resistance mechanisms, however, may differ. For example, the coarse Qtz–slide may dissipate more energy during erosion due to higher internal friction in the coarse beds (Table 1). Flume experiments have shown that coarse sediments exhibit greater resistance to erosion . This could offset any tendency toward higher flow-front velocities of the coarse debris flows during this phase, and result in comparable velocities to the fine debris flows by the end of the erosive section. The reference scenarios support this interpretation. Under identical basal conditions along the entire flume channel, the coarse debris flows eventually accelerate more strongly on the rigid bed and attain higher final flow-front velocities than the fine debris flows (Fig. 3). Once the debris flows then enter the common rigid runout area, coarse debris flows consistently travel farther (Fig. 4). These observations suggest that during deposition mobility and spreading are modulated by basal friction, which, on the same basal surface, is lower for coarse and higher for fine material. The fine material therefore dissipates kinetic energy more rapidly and comes to rest earlier.~~ should, however, be interpreted in the context of the contrasting stepwise and

progressive mobilization modes identified above. Frontally concentrated mobilization, for example, can produce short-lived but pronounced increases in apparent erosion rate (Zhang et al., 2026). Consequently, our rate estimates represent temporal averages but do not represent a single, uniform entrainment mechanism.

4.2 ~~Additional grain-scale controls on debris-flow mobility~~

~~Our experimental data only partly reflect the three energy regimes proposed by . While the inertially weak scenarios show the expected enhancement in mobility and runout relative to the inertially neutral scenarios, the inertially strong scenarios behave more similarly to the neutral case than anticipated (Figs. 3, 4, 5). Notably, despite an almost twofold difference in solid density between Mag and Qtz (Table 1), both scenarios produce very similar runout. This suggests that, solid density contrasts alone do not fully account for the observed mobility trends and depositional patterns among the different scenarios and that additional mechanisms acting at the grain scale may modulate the flow response and control momentum dissipation during erosion and entrainment, too. Below, we discuss the potential roles of (i) particle shape , (ii) friction, (iii) bed compaction, and (iv) particle segregation efficiency.~~

4.1.1 Particle shape and collisional effects

~~(i) Particle roundness is a key shape parameter that strongly affects the mechanical response of granular materials . Higher roundness reduces rolling resistance and~~ Particle shape further modifies bed resistance and particle transport. Greater roundness facilitates particle rotation (Estrada et al., 2011), whereas angular particles exhibit stronger interlocking and higher shear ~~strength, reducing the magnitude of rotation~~ resistance (Ali et al., 2023). ~~In our experiments, the low-density Glass beds consist of artificial particles whose rounded, nearly spherical shapes differ markedly~~ The nearly spherical Glass particles therefore differ mechanically from the angular Qtz and Mag particles (Fig. 1). ~~This geometrical material contrast suggests that, as the near-spherical Glass particles roll more easily, the Glass beds may be entrained more readily, promoting additional mobility. This interpretation is supported by the~~ Their greater rolling mobility likely facilitates both initial mobilization from the bed and subsequent transport, contributing to the higher apparent mean erosion rates and ~~higher final~~ average flow-front velocities ~~in the Glass experiments (Fig. 3). These observations agree with findings from previous erosive debris-flow experiments , where higher particle roundness in erodible beds was found to reduce debris-flow resistance and enhance entrainment rates~~ observed for the Glass beds. This interpretation is consistent with previous experiments in which greater bed-particle roundness reduced flow resistance and enhanced entrainment (Li et al., 2022).

The influence of particle shape ~~appears~~ is particularly evident in ~~the far runout of~~ Glass/c, where a dispersed frontal fringe composed ~~almost entirely~~ predominantly of coarse spherical Glass particles ~~formed~~ forms ahead of the main deposit body (Figs. 4b and 6a). ~~In contrast,~~ Glass/f~~does not form such a fringe but only a well-confined lobe (Figs. 4a and Supplement Fig. S8a). The more pronounced rolling behavior in Glass/c therefore implies that the coarse spherical particles may dissipate less energy to frictional and collisional interactions than the fine spherical particles on the same runout surface~~, in contrast, forms

a more confined lobe without a comparable fringe. This contrast suggests an additional interaction between particle shape and size. The more dispersed coarse-particle deposits may also reflect stronger collisional stresses and stress fluctuations generated as larger grains interact with the rigid runout surface, enhancing particle agitation and spreading (Choi and Goodwin, 2021).

(ii) Once the slope exceeds a critical angle of roughly half the material's angle of repose, entrainment begins to affect the flow and may increase runout by up to 40% on slopes close to the repose angle . In our experiments, the flume inclination of 37far exceeds the internal friction angles of Glassof ~30(Table 1), which required additional stabilization of the bed to

4.1.2 Bed preparation and compaction

Bed preparation may exert an additional control. Compaction reduces bed porosity and generally increases resistance to deformation and erosion (Farin et al., 2014; Bahmanpouri et al., 2021). Whereas the Qtz and Mag beds were prepared by simple infilling, the Glass beds had to be mixed with 4–5% water by mass and superficially compacted to maintain the imposed steep inclination (Sect. 2.2). The Glass bedwas therefore effectively inclined beyond its stability limit during the experiments, offering relatively little shear resistance. This low stability allowed particles to be eroded and entrained with comparatively little mechanical forcing, likely contributing to the enhanced mobility and long runout observed in the inertially weak scenarios. In contrast, imposed slope. Small spatial variations in this compaction or between repeated runs may have affected the onset and spatial pattern of erosion. The partly greater variation in runout length and symmetry among the Glass/c repetitions may reflect such differences (Supplement Fig. S7b). However, since bed compaction was not measured directly, its influence cannot be quantified.

4.1.3 Segregation and effective entrainment

Density segregation contributes to the internal friction angles of Qtz and Mag lie close to the 37flume inclination (Table 1), meaning these beds were operated near their natural stability limits. Under these conditions, the Qtz and Mag beds were comparatively resistant to disturbance, making entrainment more difficult and energetically demanding. The similarity in their frictional behavior and comparable resistance to shearing and deformation may help to explain why both materials, despite contrasting densities, display nearly identical flow evolution, erosion depths and contrasting internal deposit structures. Density differences can drive relative particle migration even when particle sizes are comparable (Tripathi and Khakhar, 2013; Gray and Ancey, 2015). In the Qtz–Glass deposits, the lighter Glass particles preferentially occur toward the deposit surface, front, and lateral margins, whereas the denser Qtz particles remain concentrated in the central deposit body (Fig. 6a). This pattern is consistent with density-driven segregation in a mixture initially formed by a denser Qtz-slide overriding a lighter Glass bed. The rounded shape and lower frictional resistance of Glass may further enhance its relative mobility and distal transport.

Material separation is less pronounced in the Qtz–Mag deposits. Mag occurs mainly in sparse basal clusters and lateral lenses and is largely absent from the deposit front (Fig. 6b). This distribution suggests that the denser Mag particles remained preferentially near the flow base after shear-driven erosion and only partly became effectively incorporated into the flow.

This distinction between erosion and effective entrainment is important because mobilized bed material does not necessarily become fully integrated into the moving mass (Zhang et al., 2026). Consequently, less high-density material may be accelerated with the flow, potentially explaining why the Mag experiments show no systematic differences from the Qtz experiments.

The observed density segregation must be distinguished from the grain-size segregation that occurs simultaneously within each experiment. This particle sorting is characterized by coarsening toward the deposit surface and front, with a finer deposit core. It is also present in the non-erosive reference deposits (see Sect. 3.2.2) and thus independent of material-density contrasts.

4.1.4 Particle-size effects

Fine- and coarse-particle experiments preserve the same relative material-dependent patterns in erosion and flow evolution. Within each scenario, final erosion depths, apparent mean erosion rates, and flow-front velocities differ only slightly between the two particle-size fractions (Fig. 3). Within the investigated particle-size fractions, particle size therefore has only a limited influence on the relative response to the different bed materials.

By contrast, deposit morphology depends strongly on particle size. The coarse-particle flows form longer, flatter, and more elongated lobes, whereas the fine-particle flows produce shorter and thicker deposits (Figs. ~~3, 4 ,~~4 and 5). ~~Interface tests further support this interpretation , showing that a Qtz layer begins to slide on a Mag bed at inclinations of 38and 39for the fine and coarse fraction, respectively. These values closely match the internal friction angles of Qtz of 37and 39, respectively (Table 1). The influence of internal friction on bed stability and entrainment may also be reflected in the observed travel angles, commonly used as an indicator of apparent friction . Our derived travel angles are systematically lower in the inertially weak scenarios compared to the neutral and strong cases (Fig. 5). This difference is particularly pronounced in the coarse experiments , where Glass/c yields travel angles of 29–30, whereas Qtz/c and Mag/c consistently exhibit values around 34. These lower travel angles may indicate overall reduced apparent friction and enhanced mobility in the inertially weak scenarios. Comparable travel angles of 28–29were reported by for dry granular flows composed of near-spherical ~4 beads, supporting the plausibility of the observed values.~~ The non-erosive references support the interpretation that this difference develops mainly during runout and deposition. Under identical basal conditions along the entire channel, the coarse-particle flows eventually accelerate more strongly on the rigid bed and attain higher final average flow-front velocities than the fine-particle flows. The greater coarse-particle runout suggests lower effective resistance during deposition, where enhanced collisional agitation may additionally lead to the partly more dispersed deposit geometry. Thus, particle size modifies the final expression of mobility more strongly than the relative erosion response does.

~~(iii) Compaction alters bedporosity and affects the shear strength and resistance of the bed. Higher levels of bed compaction have been observed to reduce the erosion depth and erosion rate . Whereas the Qtz and Mag beds were prepared by simple infilling,~~

4.2 Collision- and friction-dominated flow regimes

The evaluation of flow regimes using dimensionless numbers facilitates the comparison of different processes across experimental and natural scales. Because our experiments involve dry granular material without an interstitial fluid phase, most dimensionless numbers commonly applied to particle–fluid mixtures are not applicable here. The Savage number (Savage and Hutter, 1989; Parsons et al., 2001)

$$N_{Sav} = \frac{\rho_{solid}\dot{\gamma}^2 d_{mean}^2}{(\rho_{solid} - \rho_{water})\, gh \tan\phi \cos\theta} \tag{1}$$

provides a suitable measure for distinguishing between collision-dominated and Coulomb-frictional flow regimes. It represents the ratio of grain-collision stresses to gravitational grain-contact stresses (Iverson and Denlinger, 2001). Following Savage and Hutter (1989), grain collisions significantly affect flow dynamics at values above the threshold $N_{Sav} = 0.1$. Following Baselt et al. (2021), the shear rate is approximated assuming a linear velocity profile, $\dot{\gamma} = u/h$, the representative grain diameter d_{mean} is used, and the Savage number is calculated for the flow front based on the mean velocity and maximum flow depth at each sensor position. For the present dry granular flows, $\rho_{water} = 0$, reducing the density term to unity. Consequently, N_{Sav} is mainly controlled by particle size, flow velocity, basal friction angle, and, in particular, flow depth.

The calculated Savage numbers show that Coulomb friction dominates almost all experiments at every sensor position. All fine-particle experiments yield $0.0015 \leq N_{Sav} \leq 0.0269$, whereas the erosive coarse-particle experiments remain within $0.0068 \leq N_{Sav} \leq 0.0575$. The non-erosive coarse-particle reference yields values between 0.023 and 0.25. These values fall within the broad range reported for other laboratory experiments and field observations (e.g. Iverson and Denlinger, 2001; Zhou and Ng, 2010; De Haas et al., 2015; Sanvitale and Bowman, 2017; Lanzoni et al., 2017a; Baselt et al., 2021). Along the upper channel, the ~~low-density Glass beds required slight surficial compaction to maintain the imposed 37flume inclination. Among the coarse-Glass repetitions (Exp16–Exp18), variations in this compaction step appear to have influenced runout length and deposit symmetry (Supplement Fig. S7b). Solely Exp17 was prepared by a different person and appeared to have received less and more uneven compaction during preparation, producing the farthest and most oblique runout. We note, however, that this inference is purely observational, as compaction was not directly measured. These compaction differences may have influenced the initial entrainment of surficial Glass-bed particles and subsequently the extent of~~ Savage number generally increases as the flow accelerates. Upon entering the erodible bed, however, N_{Sav} decreases because average flow-front velocity decreases, flow depth increases, and the ~~dispersed fringe.However, the differences were not large enough to affect the overall erosion depth.~~

~~(iv)Density differences between particles can drive segregation in granular flows even when particle sizes are equal, as buoyancy and drag act to different extents on particles of contrasting density . In our experiments,~~ basal friction angle becomes larger. After leaving the erodible bed, N_{Sav} generally increases again, but remains below the threshold of 0.1 in most experiments. Only the non-erosive coarse-particle reference transitions into the collision-influenced regime. Here, N_{Sav} increases progressively along the channel, crosses into the collision-influenced regime along the lower channel, and reaches a maximum of approximately 0.25. This increase results from the combination of the larger grain diameter, increasing average flow-front velocity, lower basal friction angle, and comparatively small flow depth. This predominantly frictional regime contrasts with the more energetic,

coarse-grained experiments of Zhang et al. (2026), in which localized high shear rates and pronounced collisional fluctuations developed during flow–bed interaction. This difference is consistent with their substantially larger particles, higher flow velocities, and more impact-dominated experimental geometry. Accordingly, collisional dissipation appears to played a minor role in the present experiments, where N_{Sav} remains below the collision-influenced threshold at nearly all sensor positions and Coulomb friction dominates the bulk flow response.

4.3 Deposit geometry and mobility scaling

Laboratory experiments are inherently affected by scale effects and complete geometric and dynamic similarity with natural events is generally unattainable (Iverson and LaHusen, 1993; Iverson, 2015). Cross-scale comparison nevertheless helps to place laboratory results within the broader spectrum of gravitational mass flows. Integral measures such as inundated area and the ~~different patterns in material separation among Qtz–Glass and Qtz–Mag deposits~~ ratio of travel distance to elevation difference provide a useful basis for this cross-scale comparison (Baselt et al., 2022).

To complement the flow-regime classification (see Sect. 4.2), the deposit-scale mobility of the present experiments is compared with the compilation of laboratory experiments and natural events by Baselt et al. (2022), based on the above mentioned integral measures (Fig. 7). In this study, the inundated area A represents the sum of the planimetric channel area traversed by the flow and the planimetric deposit area on the runout surface. The total travel distance L is the projected horizontal distance from the reservoir outlet to the deposit´s center of volume, while H denotes the corresponding elevation difference. The ratio L/H expresses the bulk flow mobility and is inversely related to the travel angle, $\arctan(H/L)$ (Baselt et al., 2022).

In the volume–area comparison (Fig. ~~6)can be attributed to differences in both particle density and shape, which together control segregation efficiency during erosion, entrainment, and deposition. In the Glass experiments, low-density Glass particles initially form the erodible bed, which is overridden by the denser Qtz–slide. This represents a mechanically unstable density configuration, in which lighter particles are forced beneath heavier ones. This instability promotes strong density-driven segregation,~~ 7a), the present experiments occupy the upper end of the small-scale laboratory range and extend the existing compilation toward larger initial volumes and inundated areas. Although the initial release volume differ only slightly among the experiments, inundated areas vary to some extent. The Glass experiments occupy the uppermost positions within the present dataset because their larger erosion volumes and more extensive deposits increase the inundated area, whereas the Qtz and Mag experiments remain closely grouped. Because the abscissa represents only the initially released volume, the positions of the erosive experiments also reflect volume growth through entrainment, particularly for Glass. Nevertheless, the present data agree well with the volume–area relation of Pudasaini and Miller (2013) for a volume–area slope of $S = 25$. This relation provides a consistent trend linking small-scale with ~~denser Qtz particles migrating downward to form a basal, momentum-dominated core, while entrained Glass particles migrate upward through kinetic sieving and buoyancy. The nearly spherical shape of the Glass particles further facilitates this upward migration by reducing interlocking and rolling resistance. Consequently,Glass particles are preferentially transported toward the flow surface, margins, and front, forming Qtz–Glass deposits with sharp~~

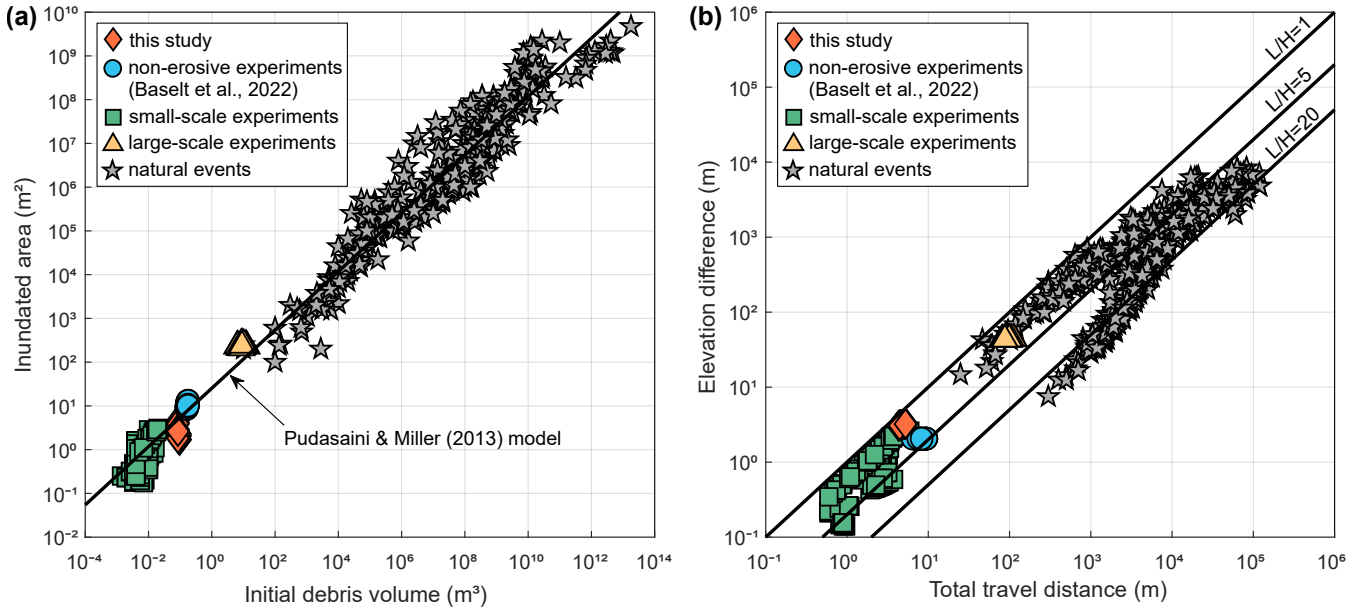


Figure 7. Evaluation of deposit geometry and mobility in comparison with other experiments and natural events. (a) Inundated area as a function of the initial debris volume and in comparison with the volume-area model by Pudasaini and Miller (2013) (volume-area slope S=25); (b) Mobility expressed as elevation difference over total travel distance. The mobility reference lines represent typical values for natural events (figure modified and extended from Baselt et al. (2022)).

~~material boundaries defined by Glass-dominated fronts and lateral edges~~ large-scale experiments and natural events (Baselt et al., 2022).

In the comparison of elevation difference and total travel distance (Fig. ~~6a). In contrast, the Mag experiments represent a mechanically stable density configuration, with~~ 7b), the ~~denser Mag particles remaining preferentially in the lower part of~~ present experiments occupy the lower-mobility end of the compilation. Nevertheless, the ~~flow once entrained. This promotes vertical density stratification but limits upward particle migration. In addition, the angularity of~~ L/H values from this study range between 1 and 5 and therefore overlap with the mobility range of many large-scale experiments and natural events. Their comparatively low position within this range is consistent with the predominantly Coulomb-frictional flow regime identified from the Savage numbers and with the dry experimental conditions. Within the present dataset, the Glass experiments attain the largest L/H values, whereas the Qtz and Mag ~~particles enhances interlocking and frictional coupling during motion, further restricting relative particle mobility. As a result, segregation in the Qtz–Mag deposits is expressed mainly as weak clustering or thin basal lenses, rather than as pronounced segregated domains (Fig. 6b).~~ experiments remain closely grouped. Their similar bulk mobility, despite their large solid-particle-density contrast, further indicates that density contrast alone does not determine runout.

4.4 Limitations and future steps

Our newly developed ~~debris-flow~~ experimental flume produced highly reproducible flow and deposition signals and robust patterns across repeated runs (Supplement Fig. S1). This provides a solid basis for testing theoretical ~~debris-flow models as well as~~ mass-flow models and for future experimental analyses of erosion and entrainment processes at the ~~slide–bed interface. Nevertheless~~flow–bed interface. Yet, certain experimental boundary conditions need to be considered when interpreting the presented results and point toward directions for future refinement and research.

The selection of ~~the~~ artificial expanded Glass as low-density material ~~for the inertially weak scenario~~ was constrained by the need for efficient post-experiment separation from Qtz and reusability~~, leading to the use of artificial expanded Glass~~. However, ~~because the Glass differs from the natural materials Qtz and Mag by its round particle shape and~~ its lower internal frictional resistance ~~, it likely has introduced additional mobility-enhancing effects beyond~~ and rounded particle shape relative to Qtz and Mag enhanced mobility beyond the intended density-related effects (see Sect. ~~4.2~~4.1.2, 4.1.1). Future experiments could explore natural alternatives with an intermediate low density, such as limestone (~1700 $\mathrm{kg\,m^{-3}}$), with comparable particle angularity and frictional behavior~~, though,~~. Though, post-experiment separation remains challenging.

~~Comparing the inertially neutral and strong scenarios, it is possible that the in-channel~~ In-channel backlog and deposition ~~obscures subtle differences~~ may obscure subtle differences between the Qtz and Mag experiments, that might otherwise become apparent under full release onto the runout area. ~~Since the flow fronts~~ Both flows entered the runout area with similar average flow-front velocities (Fig. 3) ~~and were~~ dominantly composed of Qtz particles (Fig. 6b and Supplement Fig. S8b)~~, both scenarios initially experience comparable frictional resistance~~. They therefore experienced comparable frictional conditions and rapid deceleration on the 10° inclined runout surface~~. As a result, the frontal material deposited quickly, limiting~~, causing rapid and similar frontal deposition. This may limit the visibility of possible differences at later flow stages~~. As a result, the deposits of the two scenarios may appear similar on the runout area, while any differences might~~, as these may instead be expressed in the in-channel ~~deposit, which was not analyzed with~~ deposits, which were not analyzed by 3D surface scanning. Yet, the ~~congruent temporal evolutionof flow height on the erodible bed and the similar timing and magnitude of excavation~~ near-congruent flow-height evolution, similar excavation history and erosion depths (Fig. 3) suggest that ~~the overall intensity of~~ entrainment in both scenarios ~~is~~ was broadly comparable. ~~Likewise, the nearly identical final erosion depths indicate that any differencesbetween the Qtz and Mag experiments~~Any remaining differences, if present at all, are therefore likely to be small and ~~may be~~ difficult to distinguish from the scattering that such large experimental setups naturally hold.

~~Our~~ The derived erosion rates represent apparent mean estimates ~~derived from~~ based on the final erosion depth at a single location~~(Fig. 3). These mean rates therefore~~. Therefore, they do not resolve temporal changes in erosion intensity ~~. Although the Qtz and Mag hydrographs appear nearly congruent~~(Fig. 3). Moreover, the ultrasonic measurements ~~do not allow to distinguish temporal~~ cannot distinguish changes in the elevation of the ~~slide–bed~~ flow–bed interface from changes in the thickness of the ~~overlying Qtz–slide~~overriding flow, as both contribute to the recorded flow height. Consequently, the ~~inertially neutral and strong scenarios could exhibit subtly different entrainment dynamics at the flow base~~ Qtz and Mag experiments may have

differed in their basal entrainment dynamics while still producing similar flow-height ~~curves~~records, final erosion depths, and deposit morphologies. For example, one scenario ~~might undergo~~ may have undergone shorter but more intense erosion beneath a thicker slide, whereas the other ~~erodes~~ eroded more gradually beneath a thinner slide. ~~Yet, both could yield comparable flow-height signals. Such potential temporal small-scale nuances, however,~~ Similar surface responses resulting from different combinations of basal slip, shear localization, substrate deformation, and entrainment have recently been demonstrated by Zhang et al. (2026). Comparable final erosion depths therefore do not necessarily imply identical grain-scale dynamics. Instead, differences in interface processes may compensate for each other and produce similar bulk mobility and deposit geometry, but remain inaccessible within this study. ~~To resolve such temporal processes at depth and at the grain scale, direct observations of particle motion at the erodible bed will be required. Previous studies have applied particle tracking velocimetry (PTV) to resolve the vertical velocity structure in coarse-grained flows and examine particle interactions. Over erodible beds, showed that~~

To resolve grain-scale processes hidden beneath the measured surface responses, future experiments should directly quantify particle motion and deformation across the flow–bed interface. Depth-resolved imaging methods such as Particle Tracking Velocimetry and Particle Image Velocimetry can distinguish basal sliding, localized shear, plug-like motion, and deformation from vertical velocity profiles ~~exhibit a gradual transition between coexisting rheological regimes, where frictional stresses prevail near the bed and collisional stresses dominate the upper flow region. Over rigid beds, identified distinct vertical flow regimes that control energy dissipation and mobility, with strong shear and energy expenditure concentrated at the flow base beneath a fast-moving core characterized by low shear strain rates that largely controls runout. Building on these approaches, PTV offers a means to analyze individual particle trajectories and derive~~ across the interface (e.g., Lanzoni et al., 2017b; Taylor-Noonan et al., 2022; Zhang et al., 2026). Applied to the present experimental design, these methods would directly resolve the kinematics of the flow–bed interface, allowing effective entrainment to be quantified. This is particularly relevant for the Qtz and Mag experiments, where similar surface evolution and deposit geometry may conceal different grain-scale mechanisms. Combining vertical velocity profiles ~~across the slide–bed interface . Such vertical velocity profiles would provide particle-scale quantities needed to further relate the erosion and entrainment processes in our experiments to the mechanistic descriptions of debris-flow mobility across the three energy regimes proposed by . Given the close similarity between our Qtz and Mag datasets, distinguishing these processes from natural experimental scattering will be challenging, but PTV seems promising to resolve subtle grain-scale dynamics at depth that might otherwise be obscured in our surface-based measurements.~~ with time-resolved bed lowering could clarify whether their comparable bulk response reflects similar entrainment dynamics or compensating interface processes. Such measurements would also directly relate entrainment rates to the velocity of mobilized particles entering the flow, providing a stronger basis for evaluating mass and momentum exchange across the flow–bed interface.

Finally, ~~the present~~ this study focused on dry ~~granular~~ single-phase ~~debris-flow~~ experiments to isolate the influence of ~~inertial contrasts arising solely from different solid-density material combinations. However, water is a key component of natural~~ solid-particle-density contrasts between the moving mass and the erodible bed. The experimental design was motivated by Pudasaini and Krautblatter (2021), who considered density contrast as a potential control on erosion-induced mobility changes.

Although their framework addresses landslide mobility more broadly, the present dry granular flow experiments represent its limiting case without a fluid phase and with solid volume fraction approaching unity. Natural debris flows, ~~and its presence modifies erosiondynamics, flow momentum~~ however, usually contain a fluid phase which can strongly influence erosion, momentum transfer, and mobility ~~, as demonstrated in previous experimental studies . A next step is therefore to investigate~~ (e.g., Iverson et al., 2011; De Haas and Van Woerkom, 2016; Roelofs et al., 2023). Extending the present density-contrast scnearios to two-phase ~~debris flows by recreating weak, neutral, and strong inertial contrasts through controlled variations in bed and slide water content~~ mixtures by systematically varying the water content of the moving mass and the erodible bed is therefore a logical next step. As previous studies commonly report higher erosion rates under wet or saturated conditions (Iverson et al., 2011; Reid et al., 2011; McCoy et al., 2012), such experiments could clarify whether the material-dependent trends observed here persist, weaken, or intensify in the presence of a fluid phase. ~~Moreover, previous studies indicate that erosion rate estimates often are higher if water is present , which may amplify mechanical contrasts and make subtle process differences more detectable.~~

5 Conclusions

This study experimentally ~~tested the theoretical landslide mobility model, proposed by , which predicts that inertia governs the erosion-induced momentum transfer between slide and bed and thereby debris-flow mobilityand runout. By releasing a slide of constant solid density over an erodible bed of~~ investigated the influence of solid-particle-density contrasts between a moving dry granular flow and an erodible bed on erosion, mobility, and deposition. A constant quartz slide was released over beds with lower, equal, ~~or higher solid density, we approximated inertially weak, neutral, or strong conditions to examine the effect of inertia on erosion, debris-flow mobility, and runout based on measurements of flow and deposit surface~~and higher solid particle density. Accompanying differences in internal friction, particle shape, and bed preparation were explicitly considered when interpreting the results. Our analyses lead ~~us~~ to the following main findings:

(i) ~~Inertially weak scenarios with low-density beds show enhanced erosion, higher~~ Solid particle density affects mass and momentum exchange across the flow-bed interface but is not the dominant control on mobility. Low-density glass beds produced stronger erosion, larger flow-volume increase, higher average flow-front velocities, and longer runout~~than inertially neutral scenarios with~~ . By contrast, equal-density ~~beds, in agreement with the model prediction of increased debris-flow mobility. In contrast, inertially strong scenarios with~~ quartz beds and high-density ~~beds do not exhibit the predicted mobility reduction. Instead, erosion, flow-front velocities, and deposit geometries are similar to those of the inertially neutral scenarios,~~ magnetite beds showed similarly low erosion, comparable flow evolution, and nearly identical deposit geometry despite the substantially ~~denser bed~~higher solid particle density of magnetite.

(ii) ~~Solid density contrast alone is therefore insufficient to explain the observed mobility and runout patterns . Particle shape and internal frictionexert a strong influence on debris-flow behavior. In the inertially weak scenarios, the spherical shape and~~ The observed patterns appear to be governed primarily by coupled material controls, particularly internal friction. Whereas the

low internal friction ~~angle of the low-density material reduce shear and rolling resistance, enhancing entrainment efficiency and mobility beyond what is expected from density contrast alone. In contrast, in the inertially neutral and strong scenarios, the angular shape and similar~~ and rounded particle shape of glass facilitated bed failure, particle mobilization, and incorporation into the moving flow, the similarly high internal friction ~~angles of the equal-density and high-density material promote stronger particle interlocking , resulting apparently in comparable debris-flow mobility~~and angular particle shape of quartz and magnetite promoted stronger interlocking and comparable resistance to erosion and entrainment.

(iii) Density and grain-size segregation influence where entrained material is transported and deposited and thereby modify the apparent mobility of the mixed flow. The lighter glass particles were preferentially transported to the deposit front and lateral margins, whereas the heavier magnetite particles remained concentrated in sparse basal clusters. Grain-size segregation occurred within all materials, with coarser particles concentrated toward the surface and front.

(iv) Repeating the experiments ~~for a sand and sand–gravel mixture shows that particle-size distribution does not affect~~ with finer sand-sized and coarser sand-to-gravel-sized particles did not change the relative patterns ~~among the inertial scenarios but mainly controls depositional spreadingthrough grain-size-dependent basal friction~~between the different bed materials. Particle size mainly affected basal resistance, collisional contributions, depositional spreading, and the internal structure of the deposits.

~~Consequently, a~~ Overall, our experiments demonstrate that contrasts in solid particle density alone cannot explain the mobility of erosive dry granular flows. Instead, mobility emerges from the interaction of multiple material properties and flow processes that control both the amount of material mobilized and the efficiency with which it is incorporated into the moving flow. However, surface-based ~~evaluation of flow~~ measurements alone cannot resolve the underlying processes at the flow-bed interface. Depth-resolved velocity profiles and ~~deposit characteristics alone is insufficient for a density-controlled interpretation of erosion-induced mobility changes. Resolving intrinsic process dynamics, such as vertical velocity profiles or tracking individual bed particles during entrainmentacross the slide–bed interface, will be necessary to identify subtle differences in entrainment mechanisms and momentum dissipation that are not detectable from bulk observations alone~~time-resolved bed deformation are therefore needed to distinguish basal slip, localized shear, progressive entrainment, and deeper substrate failure, and to directly relate entrainment to mass and momentum exchange.

Data availability. The experimental datasets of this study will be made freely available in an accompanying data publication via Open Data UniBw M upon full publication

Author contributions. IB conceived the project. KW and IB developed the conceptual design of the experimental flume. SM carried out the technical implementation of the flume. KW conducted the experiments, analyzed the data and prepared the initial draft, figures, and tables. KW and IB revised the manuscript based on the comments and edits of all co-authors.

965 *Competing interests.* The authors declare that they have no conflict of interest.

Acknowledgements. This research was funded by the Deutsche Forschungsgemeinschaft (DFG, German Research Foundation) – Project number: 522201978. Open access funding was enabled by the University of the Bundeswehr Munich. We thank the staff of the Hydraulic Laboratory for their technical support in constructing the experimental set-up and for their assistance during the experiments. We also thank the editors, the two reviewers, and the community members for their constructive and detailed feedback on the paper.

References

Aaron, J. and McDougall, S.: Rock avalanche mobility: The role of path material, Engineering Geology, 257, 105 126, https://doi.org/10.1016/j.enggeo.2019.05.003, 2019.

Adams, T., Grant, C., and Watson, H.: A simple algorithm to relate measured surface roughness to equivalent sand-grain roughness, International Journal of Mechanical Engineering and Mechatronics, 1, 66–71, https://doi.org/10.11159/ijmem.2012.008, 2012.

Ali, U., Kikumoto, M., Ciantia, M., Cui, Y., and Previtali, M.: Systematic effect of particle roundness/angularity on macro-and microscopic behavior of granular materials, Granular Matter, 25, 51, https://doi.org/10.1007/s10035-023-01341-y, 2023.

Bahmanpouri, F., Daliri, M., Khoshkonesh, A., Namin, M. M., and Buccino, M.: Bed compaction effect on dam break flow over erodible bed; experimental and numerical modeling, Journal of Hydrology, 594, 125 645, https://doi.org/10.1016/j.jhydrol.2020.125645, 2021.

Barbolini, M., Biancardi, A., Cappabianca, F., Natale, L., and Pagliardi, M.: Laboratory study of erosion processes in snow avalanches, Cold Regions Science and Technology, 43, 1–9, https://doi.org/10.1016/j.coldregions.2005.01.007, 2005.

Baselt, I., de Oliveira, G. Q., Fischer, J.-T., and Pudasaini, S. P.: Evolution of stony debris flows in laboratory experiments, Geomorphology, 372, 107 431, https://doi.org/10.1016/j.geomorph.2020.107431, 2021.

Baselt, I., de Oliveira, G. Q., Fischer, J.-T., and Pudasaini, S. P.: Deposition morphology in large-scale laboratory stony debris flows, Geomorphology, 396, 107 992, https://doi.org/10.1016/j.geomorph.2021.107992, 2022.

Berger, C., McArdell, B., and Schlunegger, F.: Direct measurement of channel erosion by debris flows, Illgraben, Switzerland, Journal of Geophysical Research: Earth Surface, 116, https://doi.org/10.1029/2010JF001722, 2011.

Choi, C. E. and Goodwin, S. R.: Effects of interactions between transient granular flows and macroscopically rough beds and their implications for bulk flow dynamics, Canadian Geotechnical Journal, 58, 1943–1960, https://doi.org/10.1139/cgj-2020-0160, 2021.

Cicoira, A., Blatny, L., Li, X., Trottet, B., and Gaume, J.: Towards a predictive multi-phase model for alpine mass movements and process cascades, Engineering Geology, 310, 106 866, https://doi.org/10.1016/j.enggeo.2022.106866, 2022.

Crosta, G. B., Imposimato, S., and Roddeman, D.: Numerical modeling of 2–D granular step collapse on erodible and nonerodible surface, Journal of Geophysical Research, 114, https://doi.org/10.1029/2008JF001186, 2009.

De Haas, T. and Van Woerkom, T.: Bed scour by debris flows: Experimental investigation of effects of debris-flow composition, Earth Surface Processes and Landforms, 41, 1951–1966, https://doi.org/10.1002/esp.3963, 2016.

De Haas, T., Braat, L., Leuven, J. R., Lokhorst, I. R., and Kleinhans, M. G.: Effects of debris flow composition on runout, depositional mechanisms, and deposit morphology in laboratory experiments, Journal of Geophysical Research: Earth Surface, 120, 1949–1972, https://doi.org/10.1002/2015JF003525, 2015.

De Haas, T., Nijland, W., De Jong, S., and McArdell, B.: How memory effects, check dams, and channel geometry control erosion and deposition by debris flows, Scientific reports, 10, 14 024, https://doi.org//10.1038/s41598-020-71016-8, 2020.

De Haas, T., McArdell, B. W., Nijland, W., Åberg, A. S., Hirschberg, J., and Huguenin, P.: Flow and Bed Conditions Jointly Control Debris–Flow Erosion and Bulking, Geophysical Research Letters, 49, e2021GL097 611, https://doi.org/10.1029/2021GL097611, 2022.

Egashira, S., Honda, N., and Itoh, T.: Experimental study on the entrainment of bed material into debris flow, Physics and Chemistry of the Earth, Part C: Solar, Terrestrial & Planetary Science, 26, 645–650, https://doi.org/10.1016/S1464-1917(01)00062-9, 2001.

Estrada, N., Azéma, E., Radjai, F., and Taboada, A.: Identification of rolling resistance as a shape parameter in sheared granular media, Physical Review E—Statistical, Nonlinear, and Soft Matter Physics, 84, 011 306, https://doi.org/10.1103/PhysRevE.84.011306, 2011.

Farin, M., Mangeney, A., and Roche, O.: Fundamental changes of granular flow dynamics, deposition, and erosion processes at high slope angles: insights from laboratory experiments, Journal of Geophysical Research: Earth Surface, 119, 504–532, https://doi.org/10.1002/2013JF002750, 2014.

Feng, Z., Fan, X., Ni, T., Deng, Y., Zou, C., Zhang, J., and Xu, Q.: How Ice Particles Increase Mobility of Rock–Ice Avalanches: Insights From Chute Flows Simulation of Granular Rock–Ice Mixtures by Discrete Element Method, Journal of Geophysical Research: Earth Surface, 128, https://doi.org/10.1029/2023JF007115, 2023.

Frank, F., McArdell, B. W., Huggel, C., and Vieli, A.: The importance of entrainment and bulking on debris flow runout modeling: examples from the Swiss Alps, Natural Hazards and Earth System Sciences, 15, 2569–2583, https://doi.org/10.5194/nhess-15-2569-2015, 2015.

Gray, J. and Ancey, C.: Particle-size and-density segregation in granular free-surface flows, Journal of Fluid Mechanics, 779, 622–668, https://doi.org/10.1017/jfm.2015.438, 2015.

Gray, J. and Thornton, A.: A theory for particle size segregation in shallow granular free-surface flows, Proceedings of the Royal Society A: Mathematical, Physical and Engineering Sciences, 461, 1447–1473, https://doi.org/10.1098/rspa.2004.1420, 2005.

Gray, J. M. N. T.: Particle Segregation in Dense Granular Flows, Annual Review of Fluid Mechanics, 50, 407–433, https://doi.org/10.1146/annurev-fluid-122316-045201, 2018.

Hungr, O. and Evans, S. G.: Entrainment of debris in rock avalanches: An analysis of a long run-out mechanism, Geological Society of America Bulletin, 116, 1240, https://doi.org/10.1130/B25362.1, 2004.

Hungr, O., McDougall, S., and Bovis, M.: Entrainment of material by debris flows, in: Debris-flow hazards and related phenomena, pp. 135–158, Springer, 2005.

Issler, D.: Dynamically consistent entrainment laws for depth-averaged avalanche models, J. Fluid Mech., 759, 701–738, https://doi.org/10.1017/jfm.2014.584, 2014.

Issler, D.: Comments on “On a Continuum Model for Avalanche Flow and Its Simplified Variants” by S. S. Grigorian and A. V. Ostroumov, Geosciences, 10, 96, https://doi.org/10.3390/geosciences10030096, 2020.

Issler, D., Gauer, P., Tregaskis, C., and Vicari, H.: Structure of equations for gravity mass flows with entrainment, Nature Communications, 15, 4613, https://doi.org/10.1038/s41467-024-48605-6, 2024.

Iverson, R. M.: Elementary theory of bed-sediment entrainment by debris flows and avalanches, Journal of Geophysical Research: Earth Surface, 117, https://doi.org/10.1029/2011JF002189, 2012.

Iverson, R. M.: Scaling and design of landslide and debris-flow experiments, Geomorphology, 244, 9–20, https://doi.org/10.1016/j.geomorph.2015.02.033, 2015.

Iverson, R. M. and Denlinger, R. P.: Flow of variably fluidized granular masses across three-dimensional terrain: 1. Coulomb mixture theory, Journal of Geophysical Research, 106, 537–552, https://doi.org/10.1029/2000JB900329, 2001.

Iverson, R. M. and LaHusen, R.: Friction in Debris Flows: Inferences from Large-scale Flume Experiments, in: Hydraulic engineering ’93, edited by Shen, H. W., pp. 1604–1609, American Society of Civil Engineers, New York, NY, ISBN 0872629201, 1993.

Iverson, R. M. and Ouyang, C.: Entrainment of bed material by Earth–surface mass flows: Review and reformulation of depth–integrated theory, Reviews of Geophysics, 53, 27–58, https://doi.org/10.1002/2013RG000447, 2015.

Iverson, R. M., Reid, M. E., Logan, M., LaHusen, R. G., Godt, J. W., and Griswold, J. P.: Positive feedback and momentum growth during debris-flow entrainment of wet bed sediment, Nature Geoscience, 4, 116–121, https://doi.org/10.1038/NGEO1040, 2011.

Jiang, Y., Song, P., Choi, C. E., and Choo, J.: Erosion and Transport of Dry Soil Bed by Collisional Granular Flow: Insights From a Combined Experimental–Numerical Investigation, Journal of Geophysical Research: Earth Surface, 128, e2023JF007 073, https://doi.org/10.1029/2023JF007073, 2023.

Johnson, C., Kokelaar, B., Iverson, R. M., Logan, M., LaHusen, R., and Gray, J.: Grain-size segregation and levee formation in geophysical mass flows, Journal of Geophysical Research: Earth Surface, 117, https://doi.org/10.1029/2011JF002185, 2012.

Kyburz, M. L., Sovilla, B., Bühler, Y., and Gaume, J.: Potential and challenges of depth-resolved three-dimensional MPM simulations: a case study of the 2019 'Salezer' snow avalanche in Davos, Annals of Glaciology, 65, e19, https://doi.org/10.1017/aog.2024.14, 2025.

Lanzoni, S., Gregoretti, C., and Stancanelli, L. M.: Coarse–grained debris flow dynamics on erodible beds, Journal of Geophysical Research: Earth Surface, 122, 592–614, https://doi.org/10.1002/2016JF004046, 2017a.

Lanzoni, S., Gregoretti, C., and Stancanelli, L. M.: Coarse-grained debris flow dynamics on erodible beds, Journal of Geophysical Research: Earth Surface, 122, 592–614, https://doi.org/10.1002/2016JF004046, 2017b.

Li, P., Hu, K., and Wang, X.: Debris flow entrainment rates in non-uniform channels with convex and concave slopes, Journal of Hydraulic Research, 56, 156–167, https://doi.org/10.1080/00221686.2017.1313321, 2018.

Li, P., Wang, J.-d., Hu, K.-h., Qiu, H.-j., and Xie, J.-l.: Experimental investigation on debris flow resistance and entrainment characteristics: effects of the erodible bed with discontinuous grading, Journal of Mountain Science, 19, 2397–2419, https://doi.org/10.1007/s11629-022-7365-y, 2022.

Liu, H., Zhao, X., Frattini, P., Crosta, G. B., De Blasio, F. V., Wan, Y., and Zhu, X.: Mobility and erosion of granular flows travelling on an erodible substrate: Insights from the small-scale flume experiments, Engineering Geology, 326, 107 316, https://doi.org/10.1016/j.enggeo.2023.107316, 2023.

Lu, P.-y., Yang, X.-g., Xu, F.-g., Hou, T.-x., and Zhou, J.-w.: An analysis of the entrainment effect of dry debris avalanches on loose bed materials, SpringerPlus, 5, 1621, https://doi.org/10.1186/s40064-016-3272-4, 2016.

Mangeney, A.: Landslide boost from entrainment, Nature Geoscience, 4, 77–78, https://doi.org/10.1038/ngeo1077, 2011.

Mangeney, A., Tsimring, L., Volfson, D., Aranson, I. S., and Bouchut, F.: Avalanche mobility induced by the presence of an erodible bed and associated entrainment, Geophysical Research Letters, 34, https://doi.org/10.1029/2007GL031348, 2007.

Mangeney, A., Roche, O., Hungr, O., Mangold, N., Faccanoni, G., and Lucas, A.: Erosion and mobility in granular collapse over sloping beds, Journal of Geophysical Research: Earth Surface, 115, https://doi.org/10.1029/2009JF001462, 2010.

McCoy, S., Kean, J. W., Coe, J. A., Tucker, G., Staley, D. M., and Wasklewicz, T.: Sediment entrainment by debris flows: In situ measurements from the headwaters of a steep catchment, Journal of Geophysical Research: Earth Surface, 117, https://doi.org/10.1029/2011JF002278, 2012.

McDougall, S. and Hungr, O.: Dynamic modelling of entrainment in rapid landslides, Canadian Geotechnical Journal, 42, 1437–1448, https://doi.org/10.1139/t05-064, 2005.

Medina, V., Hürlimann, M., and Bateman, A.: Application of FLATModel, a 2D finite volume code, to debris flows in the northeastern part of the Iberian Peninsula, Landslides, 5, 127–142, https://doi.org/10.1007/s10346-007-0102-3, 2008.

Mergili, M., Jaboyedoff, M., Pullarello, J., and Pudasaini, S. P.: Back calculation of the 2017 Piz Cengalo-Bondo landslide cascade with r.avaflow: what we can do and what we can learn, Natural Hazards and Earth System Science, 20, 505–520, https://doi.org/10.5194/nhess-20-505-2020, 2020.

Munch, J., Zhuang, Y., Dash, R. K., and Bartelt, P.: Dynamic Thermomechanical Modeling of Rock–Ice Avalanches: Understanding Flow Transitions, Water Dynamics, and Uncertainties, Journal of Geophysical Research: Earth Surface, 129, e2024JF007 805, https://doi.org/10.1029/2024JF007805, 2024.

Pandey, N. K. and Satyam, N.: Entrainment-driven morphological changes in debris flow deposits by varying water content at laboratory scale, Bulletin of Engineering Geology and the Environment, 84, 1–24, https://doi.org/10.1007/s10064-025-04241-y, 2025.

Papa, M., Egashira, S., and Itoh, T.: Critical conditions of bed sediment entrainment due to debris flow, Natural Hazards and Earth System Sciences, 4, 469–474, https://doi.org/10.5194/nhess-4-469-2004, 2004.

Parez, S. and Aharonov, E.: Long runout landslides: a solution from granular mechanics, Frontiers in Physics, 3, 80, https://doi.org/10.3389/fphy.2015.00080, 2015.

Parsons, J. D., Whipple, K. X., and Simoni, A.: Experimental study of the grain-flow, fluid-mud transition in debris flows, The Journal of Geology, 109, 427–447, 2001.

Peng, C., Li, X., Yuan, C., and Huang, Y.: Insights Into the Dynamics of Rock–Ice Avalanches From Small–Scale Experiments With Erodible Beds, Journal of Geophysical Research: Earth Surface, 130, e2025JF008 303, https://doi.org/10.1029/2025JF008303, 2025.

Pudasaini, S. P. and Fischer, J.-T.: A mechanical erosion model for two-phase mass flows, International Journal of Multiphase Flow, 132, 103 416, https://doi.org/10.1016/j.ijmultiphaseflow.2020.103416, 2020.

Pudasaini, S. P. and Krautblatter, M.: The mechanics of landslide mobility with erosion, Nature communications, 12, 6793, https://doi.org/10.1038/s41467-021-26959-5, 2021.

Pudasaini, S. P. and Miller, S. A.: The hypermobility of huge landslides and avalanches, Engineering Geology, 157, 124–132, https://doi.org/10.1016/j.enggeo.2013.01.012, 2013.

Reid, M. E., Iverson, R. M., Logan, M., Lahusen, R. G., Godt, J. W., and Griswold, J. P.: Entrainment of bed sediment by debris flows: results from large-scale experiments, Italian journal of engineering geology and environment, pp. 367–374, https://doi.org/10.4408/IJEGE.2011-03.B-042, 2011.

Rickenmann, D.: Empirical relationships for debris flows, Natural hazards, 19, 47–77, 1999.

Roelofs, L., Colucci, P., and de Haas, T.: How debris-flow composition affects bed erosion quantity and mechanisms: An experimental assessment, Earth Surface Processes and Landforms, 47, 2151–2169, https://doi.org/10.1002/esp.5369, 2022.

Roelofs, L., Nota, E. W., Flipsen, T. C., Colucci, P., and de Haas, T.: How bed composition affects erosion by debris flows—An experimental assessment, Geophysical Research Letters, 50, e2023GL103 294, https://doi.org/10.1029/2023GL103294, 2023.

Santi, P. M., DeWolfe, V. G., Higgins, J. D., Cannon, S. H., and Gartner, J. E.: Sources of debris flow material in burned areas, Geomorphology, 96, 310–321, https://doi.org/10.1016/j.geomorph.2007.02.022, 2008.

Sanvitale, N. and Bowman, E. T.: Visualization of dominant stress-transfer mechanisms in experimental debris flows of different particle-size distribution, Canadian Geotechnical Journal, 54, 258–269, https://doi.org/10.1139/cgj-2015-0532, 2017.

Savage, S. B. and Hutter, K.: The motion of a finite mass of granular material down a rough incline, Journal of Fluid Mechanics, 199, 177, https://doi.org/10.1017/S0022112089000340, 1989.

Savage, S. B. and Lun, C. K. K.: Particle size segregation in inclined chute flow of dry cohesionless granular solids, J. Fluid Mech., 189, 311–335, https://doi.org/10.1017/S002211208800103X, 1988.

Takahashi, T.: Debris flow, IAHR monograph series, Balkema, Rotterdam, ISBN 9054101040, 1991.

Takahashi, T.: Debris flow: Mechanics, prediction, and countermeasures, CRC Press, Boca Raton, Florida, second edition edn., ISBN 9781138000070, 2014.

Taylor-Noonan, A. M., Bowman, E. T., McArdell, B. W., Kaitna, R., McElwaine, J. N., and Take, W. A.: Influence of pore fluid on grain-scale interactions and mobility of granular flows of differing volume, Journal of Geophysical Research: Earth Surface, 127, e2022JF006 622, https://doi.org/10.1029/2022JF006622, 2022.

Tian, M., Hu, K.-h., Ma, C., and Lei, F.-h.: Effect of bed sediment entrainment on debris-flow resistance, Journal of Hydraulic Engineering, 140, 115–120, https://doi.org/10.1061/(ASCE)HY.1943-7900.0000805, 2014.

Tripathi, A. and Khakhar, D.: Density difference-driven segregation in a dense granular flow, Journal of Fluid Mechanics, 717, 643–669, https://doi.org/10.1017/jfm.2012.603, 2013.

Yang, D., Qiu, H., Quevedo, R. P., Liu, Y., and Glade, T.: Birchgletscher rock-ice avalanche burying the village of Blatten on 28 May 2025, Valais, Switzerland, Landslides, pp. 1–9, https://doi.org/10.1007/s10346-025-02656-y, 2025.

Zhang, S.-l., Gao, Y., Yin, Y.-p., Roelofs, L., Wang, W.-p., Hu, X.-w., and Li, B.: Erosion and entrainment in dry granular flows: Insights from large-scale experiments, Engineering Geology, 372, 108 966, https://doi.org/10.1016/j.enggeo.2026.108966, 2026.

Zheng, H., Shi, Z., Yu, S., Fan, X., Hanley, K. J., and Feng, S.: Erosion mechanisms of debris flow on the sediment bed, Water Resources Research, 57, e2021WR030 707, https://doi.org/10.1029/2021WR030707, 2021.

Zheng, H., Hu, X., Shi, Z., McArdell, B. W., and de Haas, T.: Volumetric growth of debris flow on erodible bed by basal shear and collision: Theory and observations, Earth and Planetary Science Letters, 662, 119 404, https://doi.org/10.1016/j.epsl.2025.119404, 2025.

Zhou, G. G. and Ng, C. W.: Dimensional analysis of natural debris flows, Canadian Geotechnical Journal, 47, 719–729, https://doi.org/10.1139/T09-134, 2010.

Zhu, L., Tang, X., He, S., Yang, Z., Liang, H., Lei, X., Luo, Y., and Zhang, L.: Geomorphology and Sedimentology of the Nyixoi Chongco Rock Avalanche and Implications for Emplacement Mechanisms, Journal of Geophysical Research: Earth Surface, 130, e2024JF007 666, https://doi.org/10.1029/2024JF007666, 2025.